The Journal of Chemical Physics

RESEARCH ARTICLE | AUGUST 28 2023

# Spin-orbit charge transfer from guanine and 9-methylguanine radical cations to nitric oxide radicals and the induced triplet-to-singlet intersystem crossing FREE

Jonathan Benny ; Jianbo Liu

Check for updates

*J. Chem. Phys.* 159, 085102 (2023)
https://doi.org/10.1063/5.0160921

View Online
Export Citation
CrossMark

## Articles You May Be Interested In

Guanine tautomerism revealed by UV–UV and IR–UV hole burning spectroscopy

*J. Chem. Phys.* (September 2001)

DNA adducts, genotoxicity mechanism of alkyl compounds in association with forensic dentistry

*AIP Conference Proceedings* (December 2019)

*Ab initio* study on deactivation pathways of excited 9 H -guanine

*J. Chem. Phys.* (April 2006)

04 September 2023 17:48:31

AIP Publishing

The Journal of Chemical Physics ARTICLE pubs.aip.org/aip/jcp

# Spin-orbit charge transfer from guanine and 9-methylguanine radical cations to nitric oxide radicals and the induced triplet-to-singlet intersystem crossing

Cite as: J. Chem. Phys. 159, 085102 (2023); doi: 10.1063/5.0160921
Submitted: 6 June 2023 • Accepted: 8 August 2023 •
Published Online: 28 August 2023

View Online Export Citation CrossMark

Jonathan Benny[1,2] and Jianbo Liu[1,2,a)]

## AFFILIATIONS

[1] Department of Chemistry and Biochemistry, Queens College of the City University of New York, 65-30 Kissena Blvd., Queens, New York 11367, USA
[2] The Ph.D. Program in Chemistry, The Graduate Center of the City University of New York, 365 5th Ave., New York, New York 10016, USA

[a)] **Author to whom correspondence should be addressed:** jianbo.liu@qc.cuny.edu. **Tel.:** 1-718-997-3271

04 September 2023 17:48:31

## ABSTRACT

Nitric oxide ($^{\bullet}$NO) participates in many biological activities, including enhancing DNA radiosensitivity in ionizing radiation-based radiotherapy. To help understand the radiosensitization of $^{\bullet}$NO, we report reaction dynamics between $^{\bullet}$NO and the radical cations of guanine (a 9HG$^{\bullet+}$ conformer) and 9-methylguanine (9MG$^{\bullet+}$). On the basis of the formation of 9HG$^{\bullet+}$ and 9MG$^{\bullet+}$ in the gas phase and the collisions of the radical cations with $^{\bullet}$NO in a guided-ion beam mass spectrometer, the charge transfer reactions of 9HG$^{\bullet+}$ and 9MG$^{\bullet+}$ with $^{\bullet}$NO were examined. For both reactions, the kinetic energy-dependent product ion cross sections revealed a threshold energy that is 0.24 (or 0.37) eV above the 0 K product 9HG (or 9MG) + NO$^+$ asymptote. To interrogate this abnormal threshold behavior, the reaction potential energy surface for [9MG + NO]$^+$ was mapped out at closed-shell singlet, open-shell singlet, and triplet states using density functional and coupled cluster theories. The results showed that the charge transfer reaction requires the interaction of a triplet-state surface originating from a reactant-like precursor complex $^3$[9MG$^{\bullet+}$(↑)·(↑)$^{\bullet}$NO] with a closed-shell singlet-state surface evolving from a charge-transferred complex $^1$[9MG·NO$^+$]. During the reaction, an electron is transferred from $\pi^*$ (NO) to perpendicular $\pi^*$ (9MG), which introduces a change in orbital angular momentum. The latter offsets the change in electron spin angular momentum and facilitates intersystem crossing. The reaction threshold in excess of the 0 K thermochemistry and the low charge-transfer efficiency are rationalized by the vibrational excitation in the product ion NO$^+$ and the kinetic shift arising from a long-lived triplet intermediate.

*Published under an exclusive license by AIP Publishing.* https://doi.org/10.1063/5.0160921

## I. INTRODUCTION

The oxidation potentials ($E^\circ$ vs normal hydrogen electrode, NHE) of the DNA nucleosides increase in the order of 1.29 V (guanosine) < 1.42 V (adenosine) < 1.6 V (deoxycytidine) < 1.7 V (thymidine).[1,2] In parallel, the adiabatic ionization potentials (IP) of the corresponding nucleobases and other DNA components increase in the order of 7.75 eV (guanine, abbreviated as G)[3,4] < 8.27 eV (adenine, A)[4] < 8.66 eV (cytosine, C)[4] < 8.82 eV (thymine, T)[4] in the gas phase and 4.42 eV (G)[5] < 4.81 eV (A)[5] < 4.91 eV (C)[5] < 5.05 eV (T)[5] < 8.4 ($PO_4^{3-}$)[6,7] < 8.9 ($HPO_4^{2-}$)[6,7] < 9.5 ($H_2PO_4^-$)[6,7] < 9.4–9.7 eV (deoxyribose)[7,8] in the solution. It indicates guanine as a dominant DNA target forone-electron oxidation and ionization. Pairing G with C in duplex DNA further decreases the $E^\circ$ of G by 0.3 V[9,10] and IP by 0.8 eV.[11,12] Compared to a G monomer, the $E^\circ$ of a GGG oligomer reduces by 0.3 V[13] and the IPs of the GG,[14–16] GGG[14–16] and GGGG[15] sequences reduce by 0.47, 0.68, and 0.77 eV, respectively. These facts rationalize the facile formation of the guanine radical cations (G$^{\bullet+}$) upon photoionization,[8,17] ionizing[18,19] and ion-beam radiation,[20] oxidation by DNA-binding transitional metal,[21,22] electrocatalytic oxidation,[23] photooxidation,[24] etc. In addition, holes created at other nucleobases may migrate to guanine sites,[25] rendering the formation of G$^{\bullet+}$ the ultimate trap for the oxidatively generated damage to DNA.[19]


Published under an exclusive license by AIP Publishing

The formation of $G^{\bullet+}$ initiates various DNA lesions.[26–31] An intriguing question is whether and how the $G^{\bullet+}$ lesions involve reactive oxygen species (ROS)[32] and reactive nitrogen species (RNS)[33–35] generated during pathologic events. In this regard, our laboratory has recently reported the reactions of the radical cations of guanine nucleobases, nucleosides, and base pairs with a major ROS found in biological systems—the lowest electronically excited singlet molecular oxygen ($^1O_2$).[36,37] In the present work, we expanded our research to the chemistry of $G^{\bullet+}$ with nitric oxide radicals ($^\bullet$NO). In living systems, $^\bullet$NO is produced by three nitric oxide synthase (NOS) isozymes, named endothelial (eNOS), neuronal (nNOS), and inducible NOS (iNOS).[38] eNOS and nNOS produce $^\bullet$NO at a rate of 1.2 mmol/day,[39] which serves as a neurotransmitter, modulates vasorelaxation, and inhibits platelet aggregation.[38] However, upon bacterial infection, $^\bullet$NO is produced up to 10–100 times more by the iNOS of macrophages.[40] While it adds to the host defense mechanism,[38,41,42] the overproduced $^\bullet$NO (at a local concentration of $10^4$ molecules/cell s)[43] induces oxidative and nitrative stress in cells. It damages cells via DNA base deamination,[44] strand breaks, and cross-links[43] and causes mutation,[43,45] carcinogenesis,[46–48] and tumors.[49]

The development of protection against $^\bullet$NO-generated damage requires the evaluation of implicated targets and products. $^\bullet$NO can diffuse freely through the cell membrane[50] and travel a significant distance during its lifetime of 3–30 s.[49,51,52] Throughout this timespan, $^\bullet$NO may form $N_2O_3$ (with $NO_2$),[45] $ONOO^-$ (with $O_2^-$),[53–55] and transition metal-nitrosyl,[49] which, in turn, converts guanine to 8-nitroguanine[46,53,55,56] or 8-oxoguanine.[54–57] $^\bullet$NO also directly and actively reacts with myoglobin[58] and hemoglobin[58,59] in extracellular space and non-heme iron, tyrosyl radicals, tryptophanyl radicals, and peroxyl radicals inside cells.[54,60,61] With that proviso, it is worth mentioning the enhancement effect of $^\bullet$NO on the radiosensitivity of DNA inside tumor cells in ionizing radiation-based radiotherapy.[62–72] The radiosensitization of $^\bullet$NO arises from its reactions with short-lived DNA radicals generated upon radiation.[65,68,71,73,74] However, there exist only a few studies on this subject, all of which focused on the $^\bullet$NO reactions with the $^\bullet$OH adducts of purine and pyrimidine.[68,74] To the best of our knowledge, no experiment or theoretical work has addressed the interaction between $^\bullet$NO and nucleobase radical cations directly.

The present work has investigated the charge transfer reactions of $^\bullet$NO with the radical cations of guanine ($9HG^{\bullet+}$, i.e., keto-N9H)[75] and a guanosine-mimicking compound 9-methylguanine ($9MG^{\bullet+}$ in which the methyl group mimics the nucleoside sugar). Capitalizing on the guided-ion beam tandem mass spectrometry experiment, we measured the kinetic energy-dependent product ion cross sections and determined reaction threshold energies. To help interpret the charge transfer reaction mechanism, reaction dynamics, and product energetics, we examined the reaction potential energy surfaces (PESs) at open-shell singlet, closed-shell singlet, and triplet states using density functional theory (DFT) and coupled cluster theory. The combined experimental and theoretical work allowed us to delineate the various aspects of the radical–radical reaction, including the internal conversion (IC) between an open-shell and a closed-shell singlet state, the intersystem crossing (ISC) between a triplet and a singlet spin multiplicity, and the properties of different intermediate complexes formed along the charge transfer process.

## II. EXPERIMENTAL AND THEORETICAL METHODS

### A. Chemicals, instrumentation, and experimental procedures

Deoxyguanosine (dGuo, Sigma-Aldrich, >99%), 9MG (Chemodex, >98%), $Cu(NO_3)_2$ (Alfa Aesar, 99.999%), and the $^\bullet$NO gas (Linde, >99.5%) were all obtained from commercial sources and used without further purification. Solvents were HPLC grade. Ion–molecule reactions were measured on a home-built guided-ion beam tandem mass spectrometer consisting of, in a sequential order, an electrospray ionization (ESI) source, a radio-frequency (rf) hexapole ion guide, a reactant quadrupole mass filter, a rf octopole ion guide surrounded by a scattering cell, a product quadrupole mass filter, and an electron multiplier detector. The apparatus along with the operation and data acquisition procedures was reported before.[76] Only a brief description is given in the following, emphasizing the instrumentation parameters used in the experiment.

$9HG^{\bullet+}$ and $9MG^{\bullet+}$ were produced by collision-induced intramolecular electron transfer and dissociation of $Cu^{II}$-nucleoside/nucleobase complexes, following an approach that was first developed by Chu *et al.* to form oligopeptide radical cations in the gas phase[77] and later adopted by Feketeová *et al.*[78] and Cheng and Bohme[79] to form gaseous nucleobase and nucleoside radical cations. To generate $9HG^{\bullet+}$, $Cu^{II}$-dGuo complexes were made in a 3:1 (v:v) methanol/water solution containing 0.25 mM dGuo and 0.25 mM $Cu(NO_3)_2$. The solution was electrosprayed into the ambient atmosphere at a flow rate of 0.06 ml/h, and the electrospray needle was biased at +2400 V relative to ground. Positively charged droplets entered the source chamber of the mass spectrometer through a desolvation capillary. The temperature of the capillary was maintained at 190 °C. A skimmer of 1.0 mm-diameter orifice is located 3 mm away from the end of the capillary, separating the source chamber and the hexapole ion guide for differential pumping. The capillary and the skimmer were biased at 104 and 20 V, respectively, relative to ground. The electric field formed between the end of the capillary and the skimmer cone promoted collision-induced dissociation (CID) of the $Cu^{II}$-dGuo complexes with the background gas within that region (which was maintained at a 1.6 Torr pressure). Among these complexes, $[Cu^{II}(dGuo)_3]^{\bullet2+}$ underwent redox separation and formed $[Cu^{I}(dGuo)_2]^+ + dGuo^{\bullet+}$. A fraction of the $dGuo^{\bullet+}$ ions eliminated the sugar group and produced $9HG^{\bullet+}$,[78,79] i.e., $dGuo^{\bullet+} \rightarrow 9HG^{\bullet+} + C_5H_8O_3$. This procedure produced guanine radical cations only in the O6-keto-N9H conformer without interference from other guanine conformers that would appear if a mixture of Cu(II) with free guanine were used in ESI. The intensity of the $9HG^{\bullet+}$ ion beam was $3 \times 10^5$ counts/s. Likewise, $9MG^{\bullet+}$ was produced by the dissociation of $[Cu^{II}(9MG)_3]^{\bullet+}$, and the ESI solution was prepared using equimolarity (0.25 mM) of 9MG and $Cu(NO_3)_2$ in methanol/water. The $9MG^{\bullet+}$ ion beam intensity was $4.6 \times 10^5$ counts/s.

Ions were skimmed and transported to the hexapole ion guide, which operated at a pressure of 5–10 mTorr. The hexapole was driven by a combination of rf potential and DC bias. The rf potential trapped ions in the radial direction at the time when ions were having thermalizing collisions with the background gas within the hexapole. Our previous calibration experiment[76] indicated that, after

04 September 2023 17:48:31


Published under an exclusive license by AIP Publishing

passing the hexapole, ions were focused to a well-defined kinetic energy with an average value equal to the hexapole DC bias potential, and their internal (vibrational and rotational) energies were thermalized to Maxwell–Boltzmann distributions at 310 K. In a UV–Vis action spectroscopy study of $9HG^{\bullet+}$ and $9MG^{\bullet+}$ by Dang *et al.*[80] and a multiple-photon dissociation (IRMPD) study of $9MG^{\bullet+}$ by Feketeová *et al.*,[81] $9HG^{\bullet+}$ and $9MG^{\bullet+}$ were generated via the similar redox separation reactions of Cu(II)-guanosine/9MG complexes. According to spectroscopy characterization, both $9HG^{\bullet+}$ and $9MG^{\bullet+}$ adopt the canonical O6-keto-N9H/$CH_3$ conformation although the O6-keto tautomer is energetically close to an O6-enol tautomer. One difference between the literature work and the present study is that in the works of Dang *et al.*[80] and Feketeová *et al.*,[81] Cu(II)-complexes were first mass-selected followed by CID within an ion trap at a He bath gas pressure of ~10 mTorr. In the present work, $9HG^{\bullet+}$ and $9MG^{\bullet+}$ were generated by CID of Cu(II)-complexes in the ion transfer region at a pressure of 1.6 Torr (mostly air and a small fraction of solvent). It might be possible to induce isomerization of $9HG^{\bullet+}$ and $9MG^{\bullet+}$ at a relatively high gas pressure and in the presence of solvent molecules.[82,83] We were not able to measure ion spectroscopy in the experiment but expected that the majority of $9HG^{\bullet+}$ and $9MG^{\bullet+}$ should remain in the O6-keto-N9H/$CH_3$ structure for two reasons. First, the ion beam was passed to the hexapole for thermalization with the background gas. Any high-energy isomers, if formed, would have most likely relaxed to the thermal equilibrium population at 310 K. Furthermore, we measured the base-pair CID of $[9MG{\bullet}9MG]^{\bullet+}$[84] and $[9MG{\bullet}1MC]^{\bullet+}$.[85] The comparison of the 0 K base-pair dissociation energies and the calculated energies of various base-pair structures consisting of guanine O6-keto, O6-enol, and N3-imino isomers suggested that O6-keto is the predominant tautomer presented in the ion beam.

Radical ions of interest were mass selected by the reactant quadrupole mass filter and injected into the octopole ion guide, which guided ions through an 11 cm long scattering cell filled with $^{\bullet}$NO. Similar to the hexapole, the octopole was driven by a superimposed DC potential on an rf voltage. The DC potential was used to decelerate/accelerate reactant ions at the octopole entrance to a desired kinetic energy in the laboratory frame ($E_{lab}$). The absolute zero of $E_{lab}$ and its full width at half-maximum (FWHM) were determined in a retarding potential measurement[76,86] by scanning the DC potential on the octopole. In ion–molecule collisions, $E_{lab}$ is converted to the center-of-mass collision energy ($E_{CM}$), i.e., $E_{CM} = E_{lab} \times m_{neutral}/(m_{neutral} + m_{ion})$, where $m_{neutral}$ and $m_{ion}$ are the masses of the neutral and ionic reactants, respectively. The uncertainty in the absolute scale of $E_{lab}$ was less than 0.1 eV, and the FWHM of the kinetic energy spread was 0.65 eV. These represented an uncertainty of <0.02 eV and a FWHM of 0.1 eV in the $E_{CM}$ for the reaction of $9HG^{\bullet+}/9MG^{\bullet+}$ with $^{\bullet}$NO. The reaction was studied over an $E_{CM}$ range from 0.05 to 7 eV so that both exothermic and endothermic reactions could be detected. After ion–molecule collisions, any product ions and the remaining reactant ions drifted to the end of the octopole and were refocused via a set of Einzel lenses into the product quadrupole mass filter. Ion signals were mass analyzed and registered using the pulse-counting electron multiplier.

To assure that the reaction was resulting from single ion–molecule collisions, the $^{\bullet}$NO pressure within the scattering cell was maintained at 0.023 mTorr. At this gas pressure, the probability of an ion undergoing a single collision with $^{\bullet}$NO was 4% and that for double collisions or more was <0.2%. Under this thin-target condition, reaction cross sections could be calculated from the ratio of product/reactant ion intensities (after correcting for the background ion intensities when the $^{\bullet}$NO gas was no longer directed into the scattering cell[76]), the gas pressure within the scattering cell, and the effective cell length, following the Beer–Lambert law.[87] The experiment was repeated four times to determine the standard deviation (i.e., relative uncertainty in the measurement). The uncertainty in absolute cross sections was estimated to be ≤20%. The measured cross sections did not change when the $^{\bullet}$NO pressure was increased to 0.05 mTorr, which verified the single-collision condition and thin-target approximation.

### B. Guided-ion beam data analysis

The kinetic energy dependence of the endothermic charge-transfer product ion cross sections was modeled using a modified line-of-centers (LOC) function,[88–91]

$$\sigma(E) = \sigma_0 \frac{(E_{CM} + E_{vib} + E_{rot} - E_0)^n}{E_{CM}}. \quad (1)$$

Here, $\sigma_0$ is an energy-independent scaling factor, $E_{CM}$ is as defined above, $E_{vib}$ and $E_{rot}$ are the reactant vibrational and rotational energies, $E_0$ is the 0 K reaction threshold energy, and $n$ is a fitting parameter that determines the efficiency of translational-to-internal energy transfer ($T \rightarrow E_{int}$) in collisions and therefore controls the slope of $\sigma(E)$.

The energy dependence of experimental reaction cross sections is known to be broadened by the internal and kinetic energy distributions of reactant ions and the thermal motion of neutral reactants.[92,93] To compare with the experimental cross sections, the $\sigma(E)$ function needs to be convoluted over the experimental energy broadening and kinetic factors. For this purpose, a Monte Carlo ion–molecule collision simulation program[85,94] was used to mimic experimental collisions. At each nominal $E_{CM}$, a total of 100 000 ion–molecule collisions were simulated. In these collisions, the $^{\bullet}$NO molecules were sampling a Maxwell–Boltzmann kinetic energy distribution and rotational energy at the scattering cell temperature of 300 K ($^{\bullet}$NO has negligible excited vibrational states at 300 K). The primary ions were sampling $E_{lab}$ (corresponding to the desired $E_{CM}$) with a FWHM of 0.65 eV in the laboratory frame and $E_{vib}$ and $E_{rot}$ from the normalized vibrational and rotational Maxwell–Boltzmann energy distributions at 310 K. The established energy distributions were then sampled into $\sigma(E)$ fitting. To account for kinetic shift[95] (i.e., excess energy is required to observe detectable dissociation of a product-like ion–molecule complex within the ion time-of-flight in the mass spectrometer),[96] each collision that had total energy exceeding $E_0$ was subjected to Rice–Ramsperger–Kassel–Marcus (RRKM) analysis[97] to determine if the product-like complex (see in the following) would lead to a dissociation within the ion time-of-flight (100–500 $\mu$s) or not.

A leveling-off function was used in the fitting to allow $\sigma(E)$ to reach a plateau at high $E_{CM}$. The rising curvature of $\sigma(E)$ is highly sensitive to $E_0$ and $n$, and their values were adjusted until the convoluted $\sigma(E)$ matched the experiment.

04 September 2023 17:48:31


Published under an exclusive license by AIP Publishing

### C. Electronic structure and PES calculations

Geometries of reactants, intermediates, and products were optimized using the ωB97XD functional coupled with the 6-31+G(d,p) basis set. This range-separated functional mitigated self-interaction errors and improved orbital descriptions of radical cations.[98] For relaxed PES scans, all the bond lengths and angles were optimized at each grid point except the scanning coordinate(s). DFT calculations were performed using the Gaussian 16 suite of programs.[99] To evaluate the open-shell singlet state of the reaction system, broken-symmetry (BS), unrestricted DFT calculations were carried out using the Guess = Mix option, and the initial BS electron density guess was generated by fragment wave functions with specific settings.[100] Reaction enthalpies (ΔH) were calculated at 0 K and included zero-point energies (ZPEs), which were scaled by 0.975.[101] Atomic charge and spin density were analyzed using the Natural Bond Orbital Analysis Program NBO 6.0.[102]

To assess whether spin contamination poses an issue for the DFT-calculated PESs, DFT-optimized reaction structures were subjected to T1 diagnostic and single-point energy calculation[103,104] using the domain-based local pair-natural orbital coupled-cluster single-, double- and perturbative triple-excitations method DLPNO-CCSD(T)[105] coupled with the aug-cc-pVTZ basis set. The inclusion of a perturbative correction for triple excitation in CCSD compensates for the deficiencies of a single-determinant reference to some extent. With partial inclusion of non-dynamical correlation effects, CCSD(T) may handle modest spin contamination. For closed-shell systems, CCSD(T) is considered a gold standard[106] of quantum chemistry with its accuracy comparable to experiments. The DLPNO-CCSD(T) calculations were carried out using the ORCA quantum chemistry program ver. 4.2.[107,108]

## III. EXPERIMENTAL RESULTS AND ANALYSIS

### A. Charge-transfer thresholds calculated from thermochemistry

The adiabatic IPs (corresponding to 0 K values) of 9HG and 9MG were calculated to be 7.69 and 7.53 eV, respectively, at the ωB97XD/6-31+G(d,p) level of theory and 7.78 and 7.63 eV, respectively, at the composite DLPNO-CCSD(T)/aug-cc-pVTZ//ωB97XD/6-31+G(d,p) levels. Using the CCSD(T) calculations extrapolated to the complete basis set limit (CBS), Tureček and co-workers reported a benchmark IP value of 7.97 eV for 9HG.[80,109] For comparison, the adiabatic IP of free guanine was measured to be in a range of 7.75–8.17 eV using the vacuum ultraviolet (VUV) photoionization efficiency (PIE) method.[3,4,8] Since the free guanine has four N-bonded H atoms that can potentially migrate, there existed in the gas-phase sample at least four low-energy neutral guanine tautomers (i.e., O6-keto-N9H, O6-keto-N7H, O6-enol-N9H, and O6-enol-N9H-*trans*) within a 0.1 eV energy range and another four tautomers (i.e., O6-enol-N7H, O6-keto-N7H-imino, O6-keto-N7H-imino-*cis,* and O6-keto-N7H–N3H) within 0.28 eV.[3] The range of the experimental guanine IP thus represents the contributions of different tautomers that were populated in the experiment, and the lowest PIE threshold (7.75 eV) can be reasonably assigned to the global minimum 9HG tautomer. It appears that the combined DLPNO-CCSD(T)//ωB97XD theories were able to reproduce the experimental 9HG IP most closely. No experimental IP data was available for 9MG. Since the DLPNO-CCSD(T)-calculated IP for 9HG is within 0.03 eV of the experimental data, we tend to assume a similar accuracy for the DLPNO-CCSD(T)-calculated IP for 9MG.

A high-precision adiabatic IP, 9.2643 ± 0.0005 eV, was reported for $^{\bullet}$NO in a pulsed-field ionization photoelectron (PFI-PE) experiment.[110] Based on the compiled experimental and calculated reactant and product adiabatic IP values, the 0 K thermodynamic thresholds for the charge transfer reactions are

$$9HG^{\bullet+} + {}^{\bullet}NO \rightarrow 9HG(\text{singlet}) + NO^{+}, \quad \Delta H(0\ K) = 1.51\ eV, \quad (2)$$

$$9MG^{\bullet+} + {}^{\bullet}NO \rightarrow 9MG(\text{singlet}) + NO^{+}, \quad \Delta H(0\ K) = 1.63\ eV. \quad (3)$$

Reactions (2) and (3) have only considered ground electronic-state 9HG and 9MG in the products as the triplet excited-state 9HG and 9MG lie in energy more than 3 eV higher than their singlet counterparts. As verified by the charge-transfer product ion cross sections (see in the following), there is no obvious contribution from a triplet product at higher collision energies.

### B. Guided-ion beam results

#### *1. Product ion cross sections and reaction efficiencies*

The charge transfer reactions (2) and (3) were measured over a center-of-mass $E_{CM}$ range of 0.05–7 eV. Cross sections for the product ions ($NO^+$) are presented in Fig. 1, wherein error bars represent standard deviations determined on the basis of four sets of measurements. Figure 1 also indicates, as vertical lines, the product asymptotic energies, i.e., the ΔH (0 K) for reactions (2) and (3). It can be seen that the actual cross sections rise from zero at a $E_{CM}$ close to but slightly above the 0 K product asymptotes or thermodynamic thresholds.

For both reaction systems, the charge-transfer cross section increases with increasing collision energy as we could expect for an endothermic process, and the cross section reaches a plateau at $E_{CM}$ of 6–7 eV before it declines. There is no inflection in the cross section when $E_{CM}$ reaches the threshold energy (4.7–4.9 eV) for producing $NO^+$ and the triplet excited state of 9HG or 9MG. The conclusion is that the conversion to a singlet-state product channel is exclusive. The collision cross sections ($\sigma_{collision}$) for the reaction systems were calculated using the orientation-averaged projected area method available in the IMoS program.[111,112] The molecular geometries and polarizabilities needed for the IMoS calculations were evaluated at the ωB97XD/6-31+G(d,p) level of theory. The calculated $\sigma_{collision}$ is 94 Å$^2$ for $9HG^{\bullet+}$ + $^{\bullet}$NO and 103 Å$^2$ for $9MG^{\bullet+}$ + $^{\bullet}$NO. Accordingly, the maximum charge-transfer cross sections for $9HG^{\bullet+}$ + $^{\bullet}$NO and $9MG^{\bullet+}$ + $^{\bullet}$NO have reached only 1.2% and 2.2% of their respective $\sigma_{collision}$. These percentages represent their maximum reaction efficiencies. The charge-transfer efficiency of $9MG^{\bullet+}$ with $^{\bullet}$NO is nearly twice that of $9HG^{\bullet+}$. In a previous study,[75] we compared the charge and spin distributions of $9HG^{\bullet+}$, $9MG^{\bullet+}$, and $dGuo^{\bullet+}$. All three radical cations share the same spin density distribution in that an unpaired electron is delocalized among guanine N3, C5, and C8. Charge is separated from spin, and C8–H is more positively charged than the other groups. An obvious consequence of the substitution of N9–H is reflected in the charge densities: the negative charge on N9 decreases from −0.38 at $9HG^{\bullet+}$ to −0.11 at $9MG^{\bullet+}$ and −0.06

04 September 2023 17:48:31


Published under an exclusive license by AIP Publishing

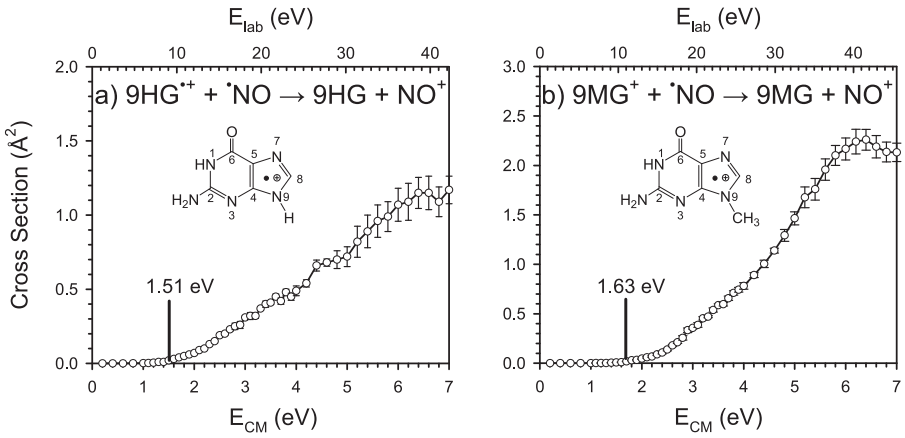


**FIG. 1.** Product ion ($NO^+$) cross sections for the charge transfer reactions of (a) $9HG^{\bullet+}$ + $^{\bullet}NO$ and (b) $9MG^{\bullet+}$ + $^{\bullet}NO$ as a function of kinetic energy in the center-of-mass frame ($E_{CM}$, bottom axis) and laboratory frame ($E_{lab}$, top axis). Circles with error bars are the experimental data, and labeled vertical lines indicate the anticipated 0 K thermodynamic threshold energies. Insets show ChemDraw for $9HG^{\bullet+}$ and $9MG^{\bullet+}$ with atom numbering schemes.

at $dGuo^{\bullet+}$; meanwhile, the charge on C4 changes from +0.10 at $9HG^{\bullet+}$ to −0.07 at $9MG^{\bullet+}$ and −0.25 at $dGuo^{\bullet+}$. These changes can be attributed to the hyperconjugation and the associated electron delocalization among the *p* orbitals of guanine and the *s* orbital of the N9-substituent. We tentatively attribute the different charge-transfer efficiencies of $9HG^{\bullet+}$ and $9MG^{\bullet+}$ to their different charge distributions.

For both reaction systems, the cross section declines slightly at the highest experimental $E_{CM}$. This decline cannot be attributed to the dissociation of product ions as the dissociation energy of $NO^+$ is 10.8 eV.[113] We tend to attribute this small decline to aberrations in the trapping and focusing of ions at high energies by the octopole ion guide and electrostatic lens; in particular, complete collection of product ions with increasingly large transverse velocity became difficult for an ion guide. Furthermore, as discussed in Sec. IV, the charge transfer reactions may be mediated by intermediate complexes. These complexes are not as efficient or long-lived at high $E_{CM}$ and thus lower the reaction efficiency.

Note that the collisions of guanine radical cations with $^{\bullet}NO$ also produced exothermic nitrosation products (i.e., covalent NO-adducts of $9HG^{\bullet+}$ and $9MG^{\bullet+}$). This will be reported in a separate paper. However, the covalent complex formation occurred only at $E_{CM}$ below 0.5 eV, which is too far below the charge-transfer threshold to be relevant.

## 2. Experimental charge-transfer threshold energies

The distribution of the reactant ion beam kinetic energy,[93] the thermal motion of $^{\bullet}NO$ molecules inside the scattering cell (i.e., Doppler broadening[92,93]), and the internal energy distributions of the ion beam and $^{\bullet}NO$ have all factored into the $E_{CM}$-threshold measurement. Consequently, the product ion cross section rises from zero at $E_{CM}$ different from the true reaction threshold (or activation) energy. To determine the true experimental threshold, the $E_{CM}$-dependent cross section was analyzed using the aforementioned LOC model. The LOC model includes all sources of energy after convolution with the kinetic energy distributions of both reactants. The model assumes that a fraction of near-threshold collisions are completely inelastic so that all of the energy contributes to overcome $E_0$.[90,91,114] Only if this assumption is true may the cross section be used to extract the reaction thermodynamic limit.

Figure 2 shows the LOC fitting for reactions (2) and (3) on a logarithmic scale. In the figure, circles represent the actual experimental data, red lines represent the LOC fits with the fitted $E_0$ marked, and blue dashed lines represent the true LOC cross sections in the absence of reactant energy broadening. For both reaction systems, the LOC model has accurately reproduced the charge-transfer cross sections over three orders of magnitude and from an energy below the threshold to 7 eV. The uncertainties of $E_0$ were determined from several independent fits using an acceptable range of $n$ (2–2.4) and included the absolute uncertainty in $E_{CM}$.

On the basis of the LOC fitting, the experimental charge-transfer threshold was determined to be 1.75 eV for $9HG^{\bullet+}$ + $^{\bullet}NO$, which exceeds the 0 K product asymptote (1.51 eV) for reaction (2) by 0.24, and 2.0 eV for $9MG^{\bullet+}$ + $^{\bullet}NO$, which exceeds the 0 K product asymptote (1.63 eV) for reaction (3) by 0.37 eV. These deviations have far exceeded the experimental uncertainty (±0.1 eV). In view of the extra 0.24–0.37 eV energy above the 0 K thermodynamic limits, questions arise as to whether there exists an actual activation barrier above the charge-transfer product asymptote, whether the LOC assumption (that some near-threshold collisions result in 100% $T \rightarrow E_{int}$) was invalid, or whether the products were formed with excess energy (i.e., not at 0 K). In fact, the latter two probabilities are not unprecedented (albeit unusual). For example, in the CID of $NO_2^+$ by Kr, the $E_0$ for dissociation to $NO^+ + O(^1D)$ was found to be 0.7 eV above the product asymptote;[115] and in collisions involving a diatomic molecule, energy can be carried away in

04 September 2023 17:48:31


Published under an exclusive license by AIP Publishing

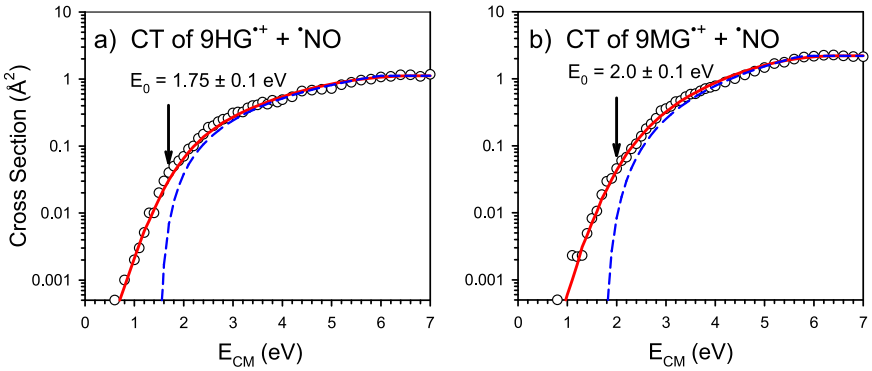


**FIG. 2.** Product ion ($NO^+$) cross sections for the charge transfer reactions of (a) $9HG^{\bullet+}$ + $^{\bullet}NO$ and (b) $9MG^{\bullet+}$ + $^{\bullet}NO$ as a function of $E_{CM}$. In each frame, black circles represent the experimental cross sections, red solid lines represent the convoluted LOC cross sections over reactant internal and kinetic energy distributions, and blue dashed lines represent the true LOC cross sections in the absence of kinetic energy distributions for reactants.

vibrational and rotational degrees of freedom, raising the reaction threshold slightly.[116]

## IV. THEORETICAL MODELING AND DISCUSSION

### A. A qualitative picture for charge transfer in perspective of the Franck–Condon principle

To explore the origin of the abnormal threshold behavior and the low reaction efficiency for the two charge transfer reactions, we turned to theoretical modeling. Compared to $9HG^{\bullet+}$, $9MG^{\bullet+}$ has a structure and distributions of spin and charge that more closely mimic those of $dGuo^{\bullet+}$, and $9MG^{\bullet+}$ presents a relatively higher charge-transfer efficiency with $^{\bullet}NO$. For these reasons, $9MG^{\bullet+}$ + $^{\bullet}NO$ was chosen as a prototypical system for PES modeling so that the theoretical results can be more reasonably extrapolated to the guanosine nucleosides in DNA. Since the equilibrium bond length (rNO) of $^{\bullet}NO$ is 1.152 Å and that of $NO^+$ is 1.068 Å, it is important to consider the charge transfer process as a function of rNO.

Figure 3 shows a schematic depiction of the NO and $NO^+$ potentials as a function of rNO from 0.9 to 1.4 Å. The potential energies were calculated at the ωB97XD/6-31+G(d,p) level of theory without ZPEs. The energy scale was adjusted so that the minima on the two potential curves are separated by the amount of the charge-transfer reaction endothermicity of 1.63 eV (=IP[NO] − IP[9MG]) for $9MG^{\bullet+}$ + $^{\bullet}NO$. Considering that at an infinite 9MG − NO separation the reaction wave function is nearly separable into 9MG and NO and the $9MG^{\bullet+}$ moiety undergoes little geometry change upon neutralization, the two potential curves can each represent the qualitative ground-state electronic surface for the reactants and products at the infinite 9MG − NO separation, i.e., the blue curve in the figure represents the $9MG^{\bullet+}$ + $^{\bullet}NO(X^2\Pi)$ charge state while the red curve represents the 9MG + $NO^+(X^1\Sigma^+)$ charge state.

Let's consider how these surfaces couple and mimic the charge transfer reaction of $9MG^{\bullet+}$ + $^{\bullet}NO$. As shown in the figure, the lowest-energy electronic state (as highlighted in yellow) is diabatic. It mixes the two charge states and thus exhibits a discontinuity around rNO = 0.95 Å. This corresponds to a change in the wave function character, i.e., a curve crossing from the $9MG^{\bullet+}$ + $^{\bullet}NO$ charge state to the 9MG + $^{+}NO$ charge state as the reactants approach each other. There is an apparent barrier of ~0.6 eV (above the adiabatic charge-transfer endothermicity) at the place where the two potential curves are likely to interact. This amount of energy allows significant "leakage" of the $^{\bullet}NO$ ($X^2\Pi$) wave function into the $NO^+$ ($X^1\Sigma^+$) potential well. This activation barrier may be understood on the basis of the Franck–Condon factor (FCF) in the ionization of $^{\bullet}NO$. A photoelectron spectroscopy study[110] reported that the direct ionization of the vibrational ground state $^{\bullet}NO$ ($X^2\Pi$, v = 0) carries significant FCFs for excitation to a long progression of vibrational excitation in $NO^+(X^1\Sigma^+)$. The FCF is 0.16 for producing $NO^+$ ($v^+ = 0$), increasing to 0.30–0.33 for producing $v^+ = 1$ and 2, declining to 0.15 for $v^+ = 3$ and 0.05 for $v^+ = 4$, and becoming negligibly small for higher $v^+$ states. It manifests a significant NO nuclear

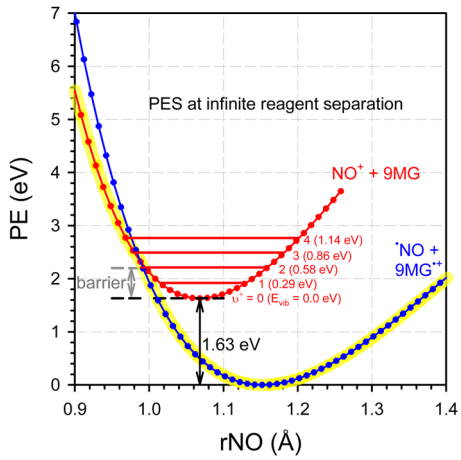


**FIG. 3.** Qualitative PESs for (blue) $9MG^{\bullet+}$ + $^{\bullet}NO(X^2\Pi)$ and (red) 9MG + $NO^+(X^1\Sigma^+)$ as a function of rNO at infinite reagent separation. Energies were calculated at the ωB97XD/6-31+G(d,p) level of theory without ZPEs. The curves were plotted so that the difference between two zero-point levels equals the charge transfer endothermicity of $9MG^{\bullet+}$ + $^{\bullet}NO$. $NO^+$ vibrational levels were taken from Ref. 110. Highlighted is the lowest-energy Bohr–Oppenheimer surface.

04 September 2023 17:48:31


Published under an exclusive license by AIP Publishing

distortion upon electron loss, and the reactant •NO may convert a fraction of reaction energy to vibrational energy in the product $NO^+$.

The above picture is too simple to quantitatively evaluate an effective threshold energy for the charge transfer reaction. The situation in the 9MG – NO complex is more complicated. First, forcing •NO into close proximity to $9MG^{\bullet+}$ changes the interaction energetics significantly, as will be shown in Sec. IV B. Second, since it is $9MG^{\bullet+}$ rather than a photon that induces the ionization of •NO, the time scale for electron loss is comparable to the time scale for nuclear motion; thus, the Franck–Condon limitation may not be fully in play in the charge-transfer reaction system. Nevertheless, such an estimate has provided a qualitative understanding of reaction energetic behavior associated with curve-crossing and $NO^+$ vibration.

### B. PESs at different electronic configurations, IC, ISC, and reaction intermediates

To fully account for the 9MG – NO interaction, relaxed PES scans were carried out for the closed-shell singlet, open-shell singlet, and triplet states of $[9MG + NO]^+$ at the ωB97XD/6-31+G(d,p) level of theory. At each state, the scan was propagating along the r[9MG – NO] coordinate, which is the center-of-mass distance between the 9MG and NO reactants. The scan continuously varied r[9MG – NO] from 30 to 1.5 Å at a step size of 0.05–0.1 Å and optimized other bond lengths and bond angles at each point. Another set of relaxed PES scans was carried out under the same conditions but along the r[9MG – N] coordinate, which is the distance between the center-of-mass of 9MG and the N-terminal of •NO. The two sets of PESs have produced nearly identical surface profiles. Because the N terminal carries the radical electron in •NO and has a much higher reactivity toward 9MG than the O terminal, r[9MG – N] represents a more appropriate coordinate than r[9MG – NO] to describe the reaction progress. The PES along the r[9MG – N] coordinate, shown in Fig. 4, was thus chosen for analysis.

Because the lowest-energy Bohr–Oppenheimer surface in the reaction energy region couples three electronic states (closed-shell singlet, open-shell singlet, and triplet), it is necessary to validate that single Slater-determinant wave functions are able to accurately describe reaction structure and electronic configuration along the reaction coordinate. To this end, we examined the values of $\langle S^2 \rangle$ in the wave function for each point. As should be expected, the $\langle S^2 \rangle$ value is 0.00 for all closed-shell singlet reaction structures and nearly 2.00 for all triplet structures. For an open-shell singlet, the $\langle S^2 \rangle$ value is 1.00 in the r[9MG – N] range from 30 to 5.7 Å, which represents a 100% diradical character evaluated using the diradical index $n_{DC} = \left(1 - \sqrt{\left(1 - \langle S^2 \rangle_{BS}\right)}\right) \times 100\%$.[100] The $\langle S^2 \rangle$ value of the singlet biradical decreases at shorter reactant separation and becomes 0.7 at r[9MG – N] = 5 Å, indicating that a singlet diradical is no longer stable upon close approaching of reactants and starts converting to a closed-shell singlet.

A more stringent test for spin contamination was carried out using the T1 diagnostic[103,104] at the DLPNO-CCSD(T)/aug-cc-pVTZ level of theory, wherein $T1 = \|t_1\|/\sqrt{n}$ (i.e., the Frobenius norm of the single-excitation amplitude vector divided by the square root of the number of electrons correlated). Empirically, a T1 diagnostic that is larger than 0.02 for a closed-shell system[104,117,118] or larger than 0.03 for an open-shell system alerts of an important

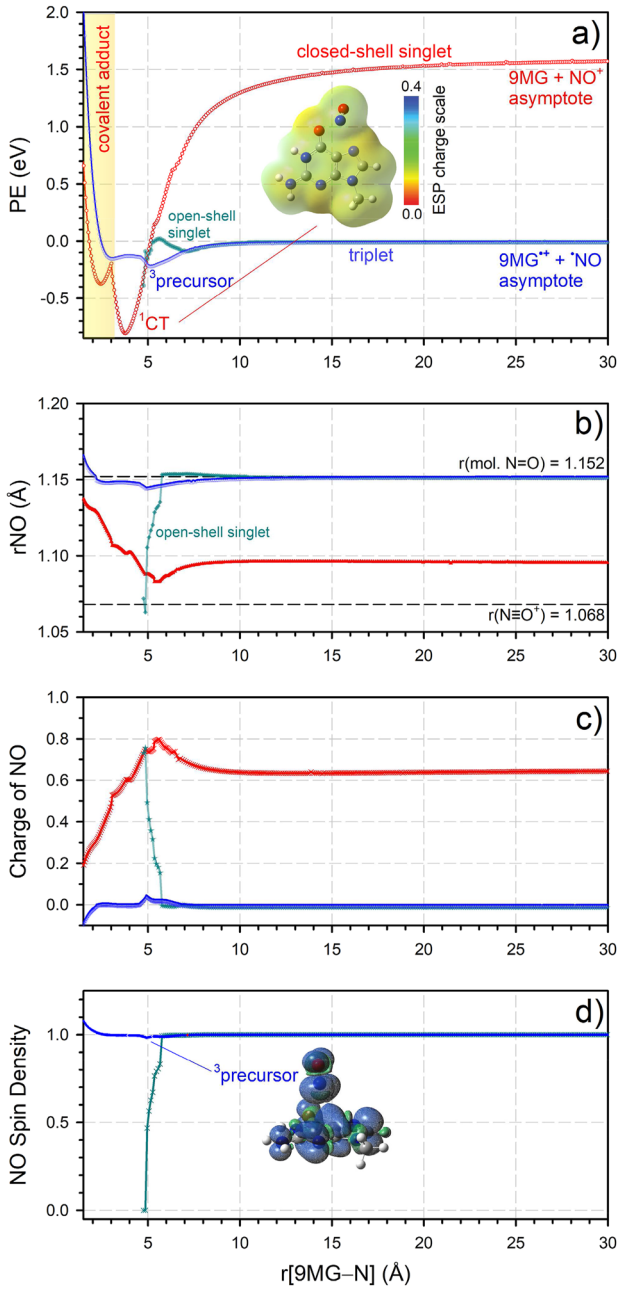


**FIG. 4.** Relaxed PES scans along r[9MG – N] (the distance between the center-of-mass of 9MG and the N-terminal of •NO) for the closed-shell singlet, open-shell singlet, and triplet states, calculated at ωB97XD/6-31+G(d,p). The color of each component is based on the electronic configuration: red for closed-shell singlet, cyan for open-shell singlet, and blue for triplet. (a) Changes in reaction potential energy (PE with respect to the sum of $9MG^{\bullet+}$ + •NO without ZPE) during the PES scan with approximate spin projection for open-shell singlet. The inset snapshot illustrates electrostatic potential (ESP)-fitted charge distribution in a $^1$CT complex (C: gray; H: white; N: blue; and O: red), and the color bar indicates charge scale; (b) the accompanying change in rNO, wherein horizontal dashed lines indicate the equilibrium rNO for molecular and ionic NO; (c) and (d) the accompanying variations in NBO charge and spin density of NO. The inset in (d) illustrates a spin density contour plot for a $^3$precursor complex.

04 September 2023 17:48:31


Published under an exclusive license by AIP Publishing

multiconfigurational character, and a T1 value above 0.06 warns of a catastrophic scenario. Figure S1 in the supplementary material summarizes the T1 diagnostic results for the closed-shell singlet, open-shell singlet, and triplet reaction structures along the reaction coordinate r[9MG − N]. All closed-shell singlet structures have the T1 value ≤0.016, and all triplet structures have the T1 value ≤0.020. Therefore, the ωB97XD/6-31+G(d,p)-calculated PESs are validated to accurately describe these two states. For open-shell singlet structures, the T1 value remains below 0.023 from r[9MG − N] = 30 to 7 Å but deteriorates at shorter distances, indicating the emergence of spin contamination. This is consistent with the $\langle S^2 \rangle$ evaluation and the analyses of rNO and the NO charge/spin density for the open-shell singlet state, as shown in Figs. 4(b)–4(d). For this reason, the open-shell singlet PES was corrected for spin contamination using Yamaguchi's approximate spin-projection method,[119,120]

$$E^{AP} = \frac{E^{BS}\langle \boldsymbol{S}^2 \rangle^{HS} - E^{HS}\langle \boldsymbol{S}^2 \rangle^{BS}}{\langle \boldsymbol{S}^2 \rangle^{HS} - \langle \boldsymbol{S}^2 \rangle^{BS}}, \tag{4}$$

where $E$ refers to electronic energy with the superscript $AP$ representing the approximately spin-projected singlet state, $BS$ is the open-shell, broken-symmetry singlet state, and $HS$ is the triplet state.

Figure 4 reports a series of theoretical predications that we have extracted from the PES scan. They are plotted in colors based on electronic configurations: red for a closed-shell singlet, cyan for an open-shell singlet, and blue for a triplet. As shown in Fig. 4(a), at long reagent separation, the open-shell singlet state presents the identical PES as that of the triplet state. Both the open-shell singlet and triplet PESs are approaching the reactant $9MG^{\bullet+}$ + $^{\bullet}NO$ asymptote while the closed-shell singlet PES is approaching the product 9MG + $NO^+$ asymptote. There are no activation barriers for the approaching of $9MG^{\bullet+}$ + $^{\bullet}NO$ at the open-shell singlet or triplet state or the separation of 9MG + $NO^+$ at the closed-shell singlet state. These observations indicate that at near-threshold energies the charge transfer reaction may be initiated at an open-shell singlet and/or a triplet surface of the radical pair [$9MG^{\bullet+}$ + $^{\bullet}NO$].

The open-shell singlet and triplet may both convert to covalently bonded NO-adducts at shorter r[9MG − N] [yellow-shaded area in Fig. 4(a)]. However, the covalent complex formation would not be in competition with charge transfer as they are located in different energy and geometrical regions.

### 1. Reaction initiated at open-shell $^1$[$9MG^{\bullet+}$ + $^{\bullet}NO$]

The PES for the open-shell singlet state [the cyan plot in Fig. 4(a)] presents no reactant interaction until the two radicals approach within a distance of 10 Å. From then on, the reactants present a small attractive potential, ranging from 0.01 eV up to 0.09 eV. This interaction is much weaker than typical ion–molecule attraction.

There appear to be two critical points along the open-shell singlet PES. The first critical point is located at r[9MG − N] = 7.0 Å below which the open-shell singlet PES starts to deviate from that of the triplet (according to the change in rNO, the deviation starts at an even larger [9MG − N] = 10 Å). Following Hund's multiplicity rule, the triple state represents the lowest-energy reactant state at a short reactant distance. The open-shell singlet may convert to the triplet at long reactant separation via an intersystem crossing process. Nevertheless, there is no driving force in the gas-phase reaction, such as a photon, heavy atom, or other stimuli, that may prompt the ISC.

The second critical point is located at r[9MG − N] = 5 Å. At this point, the open-shell singlet state converges to a closed-shell singlet via an internal conversion process [see the change in $^{\bullet}NO$ spin in Fig. 4(d)]. Along with the change in potential energy, the $^{\bullet}NO$ moiety has compressed rNO to the r($N{\equiv}O^+$) limit [Fig. 4(b)] and transferred an electron to $9MG^{\bullet+}$ [Fig. 4(c)]. There is no obvious activation barrier for the internal conversion. Without experimental measurement, we would have assigned the internal conversion of open-shell $^1$[$9MG^{\bullet+}$ + $^{\bullet}NO$] → closed-shell $^1$[9MG + $NO^+$] as the most probable pathway for charge transfer. Nevertheless, should this pathway contribute to the low-energy reaction, product ions would have been detected at the 0 K thermodynamical limit. It was not the case in the experiment. This implies that the open-shell singlet is insignificant for near-threshold energy charge transfer. This is presumably due to the extremely weak reactant attraction at the open-shell singlet, thereby rendering the formation of collision complexes inefficient. This fact may contribute to the low charge transfer reaction efficiency.

### 2. Reaction initiated at $^3$[$9MG^{\bullet+}$ + $^{\bullet}NO$]

The entrance region on the triplet PES presents long-range but small ion–dipole and ion-induced dipole interactions until the two radicals reach r[9MG − N] = 8.0 Å after which the reactant attractive potential increases with the decreasing separation. The two radicals form an electrostatically bonded ion–molecule complex (with a binding energy of 0.22 eV) at r[9MG − N] = 5 Å, i.e., collisional stabilization of reactants. The triplet radical ion-radical complex is rather floppy and does not maintain a well-defined geometry; instead, it behaves as a reactant-like precursor complex and undergoes a large amplitude of intermolecular motion. This is corroborated by the facts that at r[9MG − N] ≥ 3 Å, the NO moiety within the complex remains at a typical molecular rNO [1.15 Å, see Fig. 4(b)], its charge remains neutral, and the total spin remains at 1 [see Figs. 4(c) and 4(d)]. For this reason, the complex is referred to as a $^3$precursor complex. The significance of the $^3$precursor complex is that it correlates with the total coupled spin triplet reactants and allows repeated encounters between the reactants, so that the reactants may find an appropriate configuration for intersystem crossing to a surface that leads to a charge-transferred complex (referred to as $^1$CT, which correlates with products).

The structure of the $^1$CT complex is demonstrated in the inset of Fig. 4(a). Its Cartesian coordinates are provided in the supplementary material. The electrostatic potential (ESP)-fitted charge distributions superimposed on the $^1$CT structure illustrate an intra-complex charge transfer character. Quantitatively, the NO moiety carries a charge of 0.6 and has a bond length of 1.1 Å (which is between the molecular and ionic limits). Propagating along the exit region of the closed-shell singlet surface, the $^1$CT complex separates to 9MG + $NO^+$ as viewed by the evolution of the NO bond length and charge. There is no dissociation barrier in excess of the product 9MG + $NO^+$ asymptote. Yet, questions remain on the driving force for ISC from $^3$precursor to $^1$CT and the origin of the extra experimental threshold energy.

04 September 2023 17:48:31


Published under an exclusive license by AIP Publishing

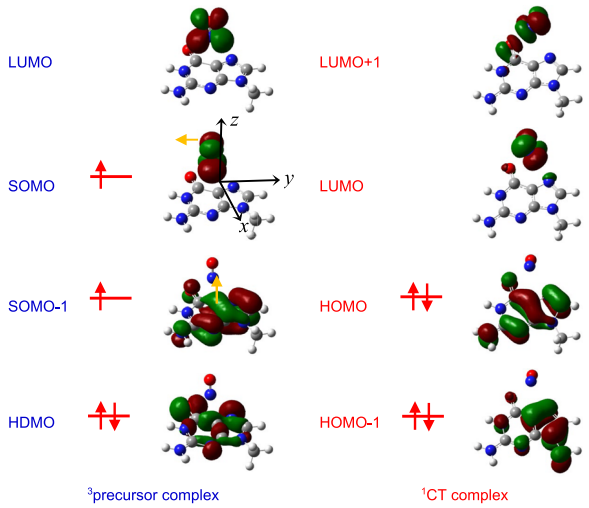


**SCHEME 1.** Molecular orbitals in a near-ISC $^3$precursor complex and singlet charge-transferred complex, calculated at the ωB97XD/6-31+G(d,p) level of theory. Red arrows indicate orbital occupancies, and yellow arrows indicate the orientation of π orbitals.

### C. Frontier molecular orbitals in the $^3$precursor-to-$^1$CT ISC

It is well known that spin–orbit coupling can facilitate mixing among electronic states of different multiplicities.[121,122] As discussed above, the $^3$precursor complex correlates adiabatically with the $9MG^{\bullet+}$ + $^{\bullet}NO$ charge state and the $^1$CT complex correlates adiabatically with the 9MG + $NO^+$ charge state. Scheme 1 illustrates the HOMO (highest occupied molecular orbital), HDMO (highest doubly occupied molecular orbital), SOMO (singly occupied molecular orbital), and LUMO (lowest unoccupied molecular orbital) in a representative $^3$precursor complex that is located near the ISC point and a $^1$CT complex. During ISC, the electron initially located in the triplet SOMO (which is composed of mostly a $\pi^*$ orbital at $^{\bullet}NO$) rephrases spin and merges into the triplet SOMO-1 (composed of mostly a $\pi^*$ orbital localized at $9MG^{\bullet+}$). With this electron transfer, the triplet SOMO and SOMO-1 become the closed-shell singlet LUMO and HOMO, respectively.

Note that the two $\pi^*$ orbitals in the triplet SOMO and SOMO-1 are orthogonal to each other. Using the right-hand rule, electron transfer between these two orbitals introduces an angular momentum change along the *x* direction. This molecular orbital angular momentum change offsets the electron spin angular momentum change. Consequently, the total angular momentum is *conserved* throughout the ISC. This process is analogous to the spin–orbit charge transfer intersystem crossing (referred to as SOCT-ISC)[123,124] that occurs in the photoexcitation of a directly connected electron donor–acceptor molecule with perpendicular π systems. The spin–orbit charge transfer could be used to justify that the ISC of $^3[9MG^{\bullet+} + {}^{\bullet}NO] \rightarrow$ closed-shell $^1[9MG + NO^+]$ is allowed, whereas the ISC of open-shell $^1[9MG^{\bullet+} + {}^{\bullet}NO] \rightarrow {}^3[9MG^{\bullet+} + {}^{\bullet}NO]$ is forbidden.

### D. Surface crossing toward charge transfer

Additional characterization of the triplet and the closed-shell singlet dynamics is provided by a more comprehensive 2D PES (Fig. 5), mapped out along r[9MG – N] and rNO. As discussed above, r[9MG – N] describes reactant approaching and product separation, while the value of rNO indicates the ionicity of the NO moiety and thus can be used to track the transition between neutral $^{\bullet}NO$ and cationic $NO^+$. The 2D PES scanned r[9MG – N] from 6.0 to 1.5 Å and rNO from 1.25 to 1.0 Å continuously with a step size of 0.05 Å for r[9MG – N] and 0.02 Å for rNO. All of the other molecular structural parameters were fully optimized at each step. The energy was plotted with respect to $9MG^{\bullet+}$ + $^{\bullet}NO$. To distinguish repulsive (or endothermic) vs attractive (or exothermic) potential, the surface is shaded in three different colors: the white-shaded stripe defines the potential regime equivalent to $9MG^{\bullet+}$ + $^{\bullet}NO$, while the blue- and yellow-shaded regimes correspond to the potential energies below and above $9MG^{\bullet+}$ + $^{\bullet}NO$, respectively.

The 2D PES profile can be summarized as follows: (1) The triplet surface presents a shallow reactant entrance valley centered at rNO of 1.14–1.15 Å. Throughout the entrance valley from

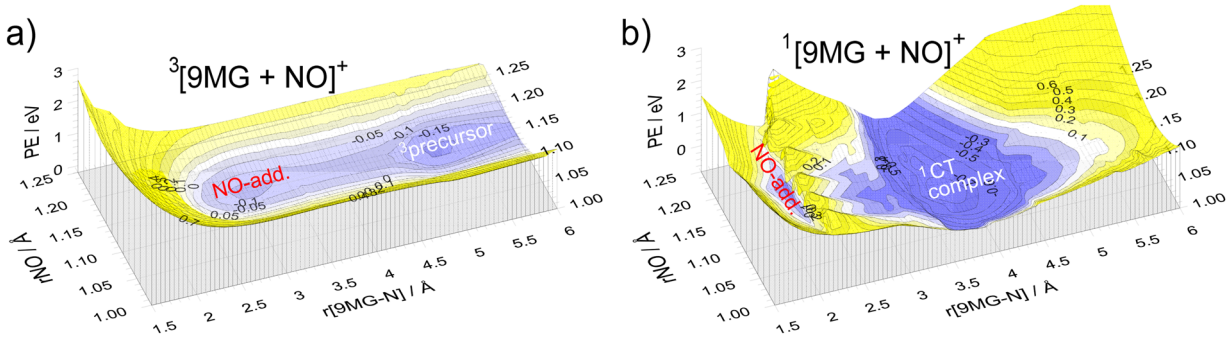


**FIG. 5.** Relaxed 2D PES scans along r[9MG – N] (the distance between the center-of-mass of 9MG and the N-terminal of $^{\bullet}NO$) and rNO for the total coupled spin (a) triplet and (b) closed-shell singlet states, calculated at the ωB97XD/6-31+G(d,p) level of theory. Numbers in contour maps are electronic energies with respect to the $9MG^{\bullet+}$ + $^{\bullet}NO$ asymptote.

04 September 2023 17:48:31


Published under an exclusive license by AIP Publishing

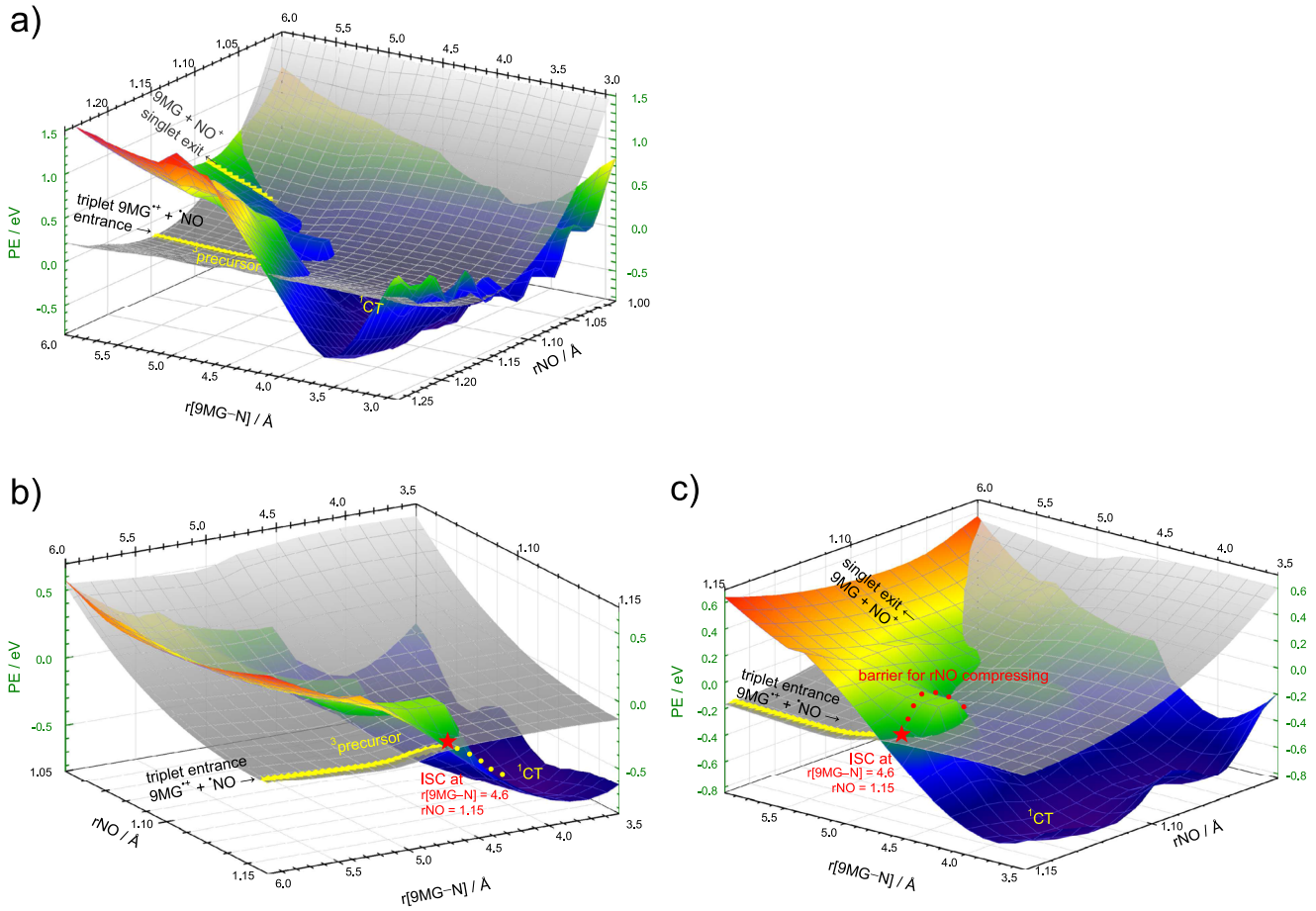


**FIG. 6.** Different views of surface crossing and post-ISC pathways, calculated at the ωB97XD/6-31+G(d,p) level of theory. The pathway in (b) leads to vibrational excitation in product $NO^+$, and the pathway in (c) leads to an activation barrier and kinetic shift of the $^3$precursor complex.

r[9MG − N] = 6 to 2.5 Å, the system maintains $9MG^{\bullet+}$ and $^{\bullet}NO$ electronic configurations. Within the entrance valley, there exist two potential wells: the deep potential well at r[9MG − N] = 5.2 Å represents the $^3$precursor complex, and the shallow potential well at r[9MG − N] = 3 Å represents covalent bond formation between $9MG^{\bullet+}$ and $^{\bullet}NO$. There is no potential barrier leading to the formation of the $^3$precursor or the covalent complex. (2) The closed-shell singlet surface is featured by a large and deep potential well centering at r[9MG − N] = 3.8 Å and rNO = 1.1 Å. This potential well corresponds to the formation of the $^1$CT complex. The closed-shell singlet surface has another, narrower potential well at r[9MG − N] = 2.3 Å and rNO = 1.13 Å, which corresponds to the formation of a covalent adduct of NO − $9MG^+$. Both potential wells have presented intracomplex charge transfer. The dissociation product exit of the $^1$CT complex is repulsive; but there is no reverse barrier above the product asymptote; in addition, there exist pathway(s) leading from $^1$CT to the covalently bonded NO − 9MG via a ridge peaked at r[9MG − N] = 2.6 Å.

Figure 6(a) represents a bird's-eye view of the closed-shell singlet 2D PES superimposed on the triplet one. Since our focus is on the reactant entrance and product exit, only the region of r[9MG − N] from 6.0 to 3.0 Å is shown for clarity. The trajectories highlighted in yellow represent the minimum-energy reactant entrance pathway, which passes through a $^3$precursor complex, and the exit pathway, which leads to 9MG + $NO^+$. Note that the minimum-energy pathway on the PES has not taken into account dynamical effects arising from finite atomic momenta. The discrepancy between experimental and theoretical threshold energy suggests that the reaction has deviated from the minimum-energy exit pathway.

To locate ISC and subsequent exit pathway(s), we examined various locations along the hypersurface seam and identified the most plausible ISC position at r[9MG − N] = 4.6 Å and rNO = 1.15 Å [indicated by a red star in Figs. 6(b) and 6(c)]. There may exist two different post-ISC pathways: (1) Fig. 6(b) has zoomed in on the first plausible pathway. Following ISC, the singlet system propagates downhill along the descending r[9MG − N] coordinate but keeps rNO = 1.15 throughout toward a $^1$CT complex (as indicated by the yellow dots). (2) The second plausible pathway may be visualized in Fig. 6(c) by rotating the horizontal view of the surfaces.

04 September 2023 17:48:31


Published under an exclusive license by AIP Publishing

The post-ISC trajectory propagates along the rNO coordinate from 1.15 to 1.10 Å while keeping r[9MG − N] constant. In this case, the trajectory crosses over an activation barrier and becomes kinetically unfavorable.

In the CID reactions of some strongly bound species, inefficient $T \rightarrow E_{int}$ transfer may result in an observed threshold higher than the thermodynamic threshold.[116] However, in the present case, neither $^3$precursor nor $^1$CT has a strong binding energy. On the other hand, if either of the two proposed post-ISC pathways is in play, it would explain why the reaction occurs at an energy higher than the 0 K product endothermicity. Following the first post-ISC pathway, the system maintains rNO at 1.15 Å in the singlet-state charge-transferred complex. As 9MG and $NO^+$ separate, their interaction becomes weak, and there are no other modes that couple with the internuclear motion of $NO^+$. Therefore, the product $NO^+$ maintains a nuclear displacement from the equilibrium bond length (1.068 Å), and the extra 0.24–0.37 eV energy nearly matches the $v^+ = 1$ excitation energy (0.29 eV) of $NO^+$.[110] This is consistent with the discussion of Franck–Condon factors in Sec. IV A.

Alternatively, in the second post-ISC pathway, the system needs to cross over a saddle point with respect to the $^3$precursor complex. This step may become rate-limiting for the charge transfer reaction. The ion time-of-flight within the mass spectrometer is 100–500 $\mu$s. Should a long-lived triplet complex form, excess energy is required to drive ISC fast enough so that collision complex dissociation may be observed in the time frame of the measurement. This kinetic shift was not included in our LOC fitting as our experiment was not able to determine the complex lifetime, and the calculation of the $^3$precursor lifetime is beyond the scope of this work. The present scenario is reminiscent of the spin–orbit charge transfer ISC in an electron donor–acceptor complex. In the latter system, a weakly coupled, triplet excited radical ion-pair is often extremely long-lived with a lifetime up to 2–6 × $10^2$ $\mu$s.[124–128] We hope that this experimental result will stimulate interest in the future theoretical studies of the $^3$precursor complex. We also note that at sufficiently high $E_{CM}$, the collision complex dissociation model is likely to become insignificant, which may explain the declining cross section at the highest $E_{CM}$.

## V. CONCLUSIONS

A guided-ion beam study was carried out to examine the interactions of $^{\bullet}$NO with $9HG^{\bullet+}$ and $9MG^{\bullet+}$, focusing on the charge transfer reactions between the collision partners. The measurement of kinetic energy-dependent product ion cross sections revealed that both reaction systems produce charge transfer products at the singlet spin multiplicity exclusively, and no triplet product was discernible. The reaction threshold energies (after correcting for reactant energy broadening) are 1.75 eV for $9HG^{\bullet+}$ + $^{\bullet}$NO → 9HG + $NO^+$ and 2.00 eV for $9MG^{\bullet+}$ + $^{\bullet}$NO → 9MG + NO, which exceed the respective 0 K product asymptotes by 0.24 and 0.37 eV. Reaction PESs at the closed-shell singlet, open-shell singlet, and triplet states as well as frontier molecular orbitals were explored to characterize the changes in reaction structure, charge, spin, and energy during the charge transfer reaction. The reaction at the near-threshold energy range involves several steps: long-range ion–dipole and ion-induced dipole attraction lead to the formation of an electrostatically bonded $^3[G^{\bullet+}(\uparrow)\bullet(\uparrow)^{\bullet}NO]$ precursor complex in ion–molecule collisions; the precursor complex may be sufficiently long lived such that spin–orbit charge transfer intersystem crossing occurs to form a charge-transferred $^1[G(\uparrow\downarrow)\bullet NO^+]$ complex; with sufficient $T \rightarrow E_{int}$, the $^1[G(\uparrow\downarrow)\bullet NO^+]$ complex proceeds along the product exit channel to the endothermic G + $NO^+$ asymptote with no reverse activation barrier. The reaction threshold in excess of the 0 K product asymptote is most likely due to the combination of the kinetic shift of the long-lived $^3[G^{\bullet+}(\uparrow)\bullet(\uparrow)^{\bullet}NO]$ complex and the vibrational excitation in the product $NO^+$. This work illustrates the chemistry of guanine nucleobases upon one-electron oxidation and subsequently the reaction with $^{\bullet}$NO. The findings are of interest in biological systems wherein $^{\bullet}$NO is produced as the precursor of reactive nitrogen species and in ionizing radiation-based radiotherapy wherein $^{\bullet}$NO is being used as a radiosensitizer to damage tumor DNA. $^{\bullet}$NO is also produced by solar photolysis and auroral activity in the upper mesosphere and lower thermosphere regions.[129,130] With the formation and ionization of guanine in space (e.g., under prebiotic conditions[131] and in carbonaceous meteorites[132]), the titled reaction might be relevant therein.

## SUPPLEMENTARY MATERIAL

Cartesian coordinates of the $^1$CT complex and T1 diagnostics of DFT-calculated PESs.

## ACKNOWLEDGMENTS

This work was supported by National Science Foundation (Grant No. CHE 1856362). J.B. acknowledges the CUNY Graduate Center Dissertation Fellowship.

## AUTHOR DECLARATIONS

### Conflict of Interest

The authors have no conflicts to disclose.

### Author Contributions

**Jonathan Benny**: Conceptualization (equal); Data curation (equal); Formal analysis (equal); Funding acquisition (equal); Investigation (equal); Methodology (equal); Project administration (equal); Resources (equal); Software (equal); Validation (equal); Writing – original draft (equal); Writing – review & editing (equal). **Jianbo Liu**: Conceptualization (lead); Data curation (supporting); Formal analysis (equal); Funding acquisition (equal); Investigation (equal); Methodology (equal); Project administration (lead); Resources (lead); Software (equal); Supervision (lead); Validation (equal); Writing – original draft (lead); Writing – review & editing (lead).

## DATA AVAILABILITY

The data that support the findings of this study are available within the article and its supplementary material.

04 September 2023 17:48:31


Published under an exclusive license by AIP Publishing

## REFERENCES


[1] S. Steenken and S. V. Jovanovic, "How easily oxidizable is DNA? One-electron reduction potentials of adenosine and guanosine radicals in aqueous solution," J. Am. Chem. Soc. **119**, 617–618 (1997).

[2] C. J. Burrows and J. G. Muller, "Oxidative nucleobase modifications leading to strand scission," Chem. Rev. **98**, 1109–1151 (1998).

[3] J. Zhou, O. Kostko, C. Nicolas, X. Tang, L. Belau, M. S. de Vries, and M. Ahmed, "Experimental observation of guanine tautomers with VUV photoionization," J. Phys. Chem. A **113**, 4829–4832 (2009).

[4] M. Schwell and M. Hochlaf, "Photoionization spectroscopy of nucleobases and analogues in the gas phase using synchrotron radiation as excitation light source," Top. Curr. Chem. **355**, 155–208 (2015).

[5] C. E. Crespo-Hernández, R. Arce, Y. Ishikawa, L. Gorb, J. Leszczynski, and D. M. Close, "Ab initio ionization energy thresholds of DNA and RNA bases in gas phase and in aqueous solution," J. Phys. Chem. A **108**, 6373–6377 (2004).

[6] E. Pluharova, M. Oncak, R. Seidel, C. Schroeder, W. Schroeder, B. Winter, S. E. Bradforth, P. Jungwirth, and P. Slavicek, "Transforming anion instability into stability: Contrasting photoionization of three protonation forms of the phosphate ion upon moving into water," J. Phys. Chem. B **116**, 13254–13264 (2012).

[7] C. A. Schroeder, E. Pluharova, R. Seidel, W. P. Schroeder, M. Faubel, P. Slavicek, B. Winter, P. Jungwirth, and S. E. Bradforth, "Oxidation half-reaction of aqueous nucleosides and nucleotides via photoelectron spectroscopy augmented by ab initio calculations," J. Am. Chem. Soc. **137**, 201–209 (2015).

[8] L. P. Candeias and S. Steenken, "Ionization of purine nucleosides and nucleotides and their components by 193-nm laser photolysis in aqueous solution: Model studies for oxidative damage of DNA," J. Am. Chem. Soc. **114**, 699–704 (1992).

[9] T. Caruso, M. Carotenuto, E. Vasca, and A. Peluso, "Direct experimental observation of the effect of the base pairing on the oxidation potential of guanine," J. Am. Chem. Soc. **127**, 15040–15041 (2005).

[10] C. E. Crespo-Hernández, D. M. Close, L. Gorb, and J. Leszczynski, "Determination of redox potentials for the Watson–Crick base pairs, DNA nucleosides, and relevant nucleoside analogues," J. Phys. Chem. B **111**, 5386–5395 (2007).

[11] M. Hutter and T. Clark, "On the enhanced stability of the Guanine–Cytosine base-pair radical cation," J. Am. Chem. Soc. **118**, 7574–7577 (1996).

[12] H. M. Jaeger and H. F. Schaefer III, "Characterizing radiation-induced oxidation of DNA by way of the monohydrated Guanine–Cytosine radical cation," J. Phys. Chem. B **113**, 8142–8148 (2009).

[13] A. Kumar, A. Adhikary, M. D. Sevilla, and D. M. Close, "One-electron oxidation of ds(5′-GGG-3′) and ds(5′-G(8OG)G-3′) and the nature of hole distribution: A density functional theory (DFT) study," Phys. Chem. Chem. Phys. **22**, 5078–5089 (2020).

[14] I. Saito, M. Takayama, H. Sugiyama, K. Nakatani, A. Tsuchida, and M. Yamamoto, "Photoinduced DNA cleavage via electron transfer: Demonstration that guanine residues located 5′ to guanine are the most electron-donating sites," J. Am. Chem. Soc. **117**, 6406–6407 (1995).

[15] H. Sugiyama and I. Saito, "Theoretical studies of GG-specific photocleavage of DNA via electron transfer: Significant lowering of ionization potential and 5′-localization of HOMO of stacked GG bases in B-form DNA," J. Am. Chem. Soc. **118**, 7063–7068 (1996).

[16] I. Saito, T. Nakamura, K. Nakatani, Y. Yoshioka, K. Yamaguchi, and H. Sugiyama, "Mapping of the hot spots for DNA damage by one-electron oxidation: Efficacy of GG doublets and GGG triplets as a trap in long-range hole migration," J. Am. Chem. Soc. **120**, 12686–12687 (1998).

[17] D. N. Nikogosyan, "Two-quantum UV photochemistry of nucleic acids: Comparison with conventional low-intensity UV photochemistry and radiation chemistry," Int. J. Radiat. Biol. **57**, 233–299 (1990).

[18] L. P. Candeias and S. Steenken, "Structure and acid-base properties of one-electron-oxidized deoxyguanosine, guanosine, and 1-methylguanosine," J. Am. Chem. Soc. **111**, 1094–1099 (1989).

[19] S. Steenken, "Purine bases, nucleosides, and nucleotides: Aqueous solution redox chemistry and transformation reactions of their radical cations and $e^-$ and OH adducts," Chem. Rev. **89**, 503–520 (1989).

[20] M. Kant, P. Jaruga, E. Coskun, S. Ward, A. D. Stark, T. Baumann, D. Becker, A. Adhikary, M. D. Sevilla, and M. Dizdaroglu, "Ne-22 ion-beam radiation damage to DNA: From initial free radical formation to resulting DNA-base damage," ACS Omega **6**, 16600–16611 (2021).

[21] I. Saito, T. Nakamura, and K. Nakatani, "Mapping of highest occupied molecular orbitals of duplex DNA by cobalt-mediated guanine oxidation," J. Am. Chem. Soc. **122**, 3001–3006 (2000).

[22] E. D. A. Stemp and J. K. Barton, "Electron transfer between metal complexes bound to DNA: Is DNA a wire?," Met. Ions Biol. Syst. 33, 325–365 (1996).

[23] H. Holden Thorp, "Cutting out the middleman: DNA biosensors based on electrochemical oxidation," Trends Biotechnol. **16**, 117–121 (1998).

[24] H. Kasai, Z. Yamaizumi, M. Berger, and J. Cadet, "Photosensitized formation of 7,8-dihydro-8-oxo-2′-deoxyguanosine (8-hydroxy-2′-deoxyguanosine) in DNA by riboflavin: A nonsinglet oxygen-mediated reaction," J. Am. Chem. Soc. **114**, 9692–9694 (1992).

[25] F. D. Lewis, X. Liu, J. Liu, S. E. Miller, R. T. Hayes, and M. R. Wasielewski, "Direct measurement of hole transport dynamics in DNA," Nature **406**, 51–53 (2000).

[26] J. Cadet, T. Douki, and J.-L. Ravanat, "Oxidatively generated base damage to cellular DNA," Free Radical Biol. Med. **49**, 9–21 (2010).

[27] J. Cadet and J. R. Wagner, "DNA base damage by reactive oxygen species, oxidizing agents, and UV radiation," Cold Spring Harbor Perspect. Biol. **5**, a012559 (2013).

[28] W. L. Neeley and J. M. Essigmann, "Mechanisms of formation, genotoxicity, and mutation of guanine oxidation products," Chem. Res. Toxicol. **19**, 491–505 (2006).

[29] A. M. Fleming and C. J. Burrows, "Formation and processing of DNA damage substrates for the hNEIL enzymes," Free Radical Biol. Med. **107**, 35–52 (2017).

[30] D. Becker and M. D. Sevilla, in *Advances in Radiation Biology*, edited by J. T. Lett and W. K. Sinclair (Academic Press, Inc., San Diego, CA, 1993), pp. 121–180.

[31] M. D. Sevilla, D. Becker, A. Kumar, and A. Adhikary, "Gamma and ion-beam irradiation of DNA: Free radical mechanisms, electron effects, and radiation chemical track structure," Radiat. Phys. Chem. **128**, 60–74 (2016).

[32] D. T. Sawyer, *Oxygen Chemistry* (Oxford University Press, New York, 1991).

[33] C. Szabó and H. Ohshima, "DNA damage induced by peroxynitrite: Subsequent biological effects," Nitric Oxide **1**, 373–385 (1997).

[34] J. Tuo, L. Liu, H. E. Poulsen, A. Weimann, O. Svendsen, and S. Loft, "Importance of guanine nitration and hydroxylation in DNA in vitro and in vivo," Free Radical Biol. Med. **29**, 147–155 (2000).

[35] Y. Terasaki, T. Akuta, M. Terasaki, T. Sawa, T. Mori, T. Okamoto, M. Ozaki, M. Takeya, and T. Akaike, "Guanine nitration in idiopathic pulmonary fibrosis and its implication for carcinogenesis," Am. J. Respir. Crit. Care Med. **174**, 665–673 (2006).

[36] Y. Sun, M. Tsai, M. M. Moe, and J. Liu, "Dynamics and multiconfiguration potential energy surface for the singlet $O_2$ reactions with radical cations of guanine, 9-methylguanine, 2′-deoxyguanosine, and guanosine," J. Phys. Chem. A **125**, 1564–1576 (2021).

[37] M. M. Moe, T. Saito, M. Tsai, and J. Liu, "Singlet $O_2$ oxidation of the radical cation versus the dehydrogenated neutral radical of 9-methylguanine in a Watson–Crick base pair. Consequences of structural context," J. Phys. Chem. B **126**, 5458–5472 (2022).

[38] X. Garcia and F. Stein, "Nitric oxide," Semin. Pediatr. Infect. Dis. **17**, 55–57 (2006).

[39] J. H. Hotchkiss, "Nitrate, nitrite balance, and de novo synthesis of nitrate," Am. J. Clin. Nutr. **47**, 161 (1988).

[40] H. Terato, A. Masaoka, K. Asagoshi, A. Honsho, Y. Ohyama, T. Suzuki, M. Yamada, K. Makino, K. Yamamoto, and H. Ide, "Novel repair activities of alka (3-methyladenine DNA glycosylase II) and endonuclease VIII for xanthine and oxanine, guanine lesions induced by nitric oxide and nitrous acid," Nucleic Acids Res. **30**, 4975–4984 (2002).

[41] J. B. Hibbs, Jr., R. R. Taintor, Z. Vavrin, and E. M. Rachlin, "Nitric oxide: A cytotoxic activated macrophage effector molecule," Biochem. Biophys. Res. Commun. **157**, 87–94 (1988).

[42] M. A. Marletta, P. S. Yoon, R. Iyengar, C. D. Leaf, and J. S. Wishnok, "Macrophage oxidation of L-arginine to nitrite and nitrate: Nitric oxide is an intermediate," Biochemistry **27**, 8706–8711 (1988).

[43] S. Tamir, S. Burney, and S. R. Tannenbaum, "DNA damage by nitric oxide," Chem. Res. Toxicol. **9**, 821–827 (1996).


04 September 2023 17:48:31



Published under an exclusive license by AIP Publishing

[44]D. A. Wink, K. S. Kasprzak, C. M. Maragos, R. K. Elespuru, M. Misra, T. M. Dunams, T. A. Cebula, W. H. Koch, A. W. Andrews, J. S. Allen, and L. K. Keefer, "DNA deaminating ability and genotoxicity of nitric oxide and its progenitors," Science **254**, 1001–1003 (1991).
[45]T. Nguyen, D. Brunson, C. L. Crespi, B. W. Penman, J. S. Wishnok, and S. R. Tannenbaum, "DNA damage and mutation in human cells exposed to nitric oxide in vitro," Proc. Natl. Acad. Sci. U. S. A. **89**, 3030–3034 (1992).
[46]S. Kawanishi and Y. Hiraku, "Oxidative and nitrative DNA damage as biomarker for carcinogenesis with special reference to inflammation," Antioxid. Redox Signaling **8**, 1047–1058 (2006).
[47]M. Murata, R. Thanan, N. Ma, and S. Kawanishi, "Role of nitrative and oxidative DNA damage in inflammation-related carcinogenesis," J. Biomed. Biotechnol. **2012**, 623019.
[48]S. Kawanishi, S. Ohnishi, N. Ma, Y. Hiraku, S. Oikawa, and M. Murata, "Nitrative and oxidative DNA damage in infection-related carcinogenesis in relation to cancer stem cells," Genes Environ. **38**, 26 (2017).
[49]P. K. Lala and C. Chakraborty, "Role of nitric oxide in carcinogenesis and tumour progression," Lancet Oncol. **2**, 149–156 (2001).
[50]W. K. Subczynski, M. Lomnicka, and J. S. Hyde, "Permeability of nitric oxide through lipid bilayer membranes," Free Radical Res. **24**, 343–349 (1996).
[51]R. M. J. Palmer, A. G. Ferrige, and S. Moncada, "Nitric oxide release accounts for the biological activity of endothelium-derived relaxing factor," Nature **327**, 524–526 (1987).
[52]L. J. Ignarro, G. M. Buga, K. S. Wood, R. E. Byrns, and G. Chaudhuri, "Endothelium-derived relaxing factor produced and released from artery and vein is nitric oxide," Proc. Natl. Acad. Sci. U. S. A. **84**, 9265–9269 (1987).
[53]V. Yermilov, J. Rubio, M. Becchi, M. D. Friesen, B. Pignatelli, and H. Ohshima, "Formation of 8-nitroguanine by the reaction of guanine with peroxynitrite in vitro," Carcinogenesis **16**, 2045–2050 (1995).
[54]B. Halliwell, K. Zhao, and M. Whiteman, "Nitric oxide and peroxynitrite. The ugly, the uglier and the not so good," Free Radical Res. **31**, 651–669 (1999).
[55]J. C. Niles, J. S. Wishnok, and S. R. Tannenbaum, "Peroxynitrite-induced oxidation and nitration products of guanine and 8-oxoguanine: Structures and mechanisms of product formation," Nitric Oxide **14**, 109–121 (2006).
[56]N. R. Jena and P. C. Mishra, "Formation of 8-nitroguanine and 8-oxoguanine due to reactions of peroxynitrite with guanine," J. Comput. Chem. **28**, 1321–1335 (2007).
[57]L. J. Kennedy, K. Moore, Jr., J. L. Caulfield, S. R. Tannenbaum, and P. C. Dedon, "Quantitation of 8-oxoguanine and strand breaks produced by four oxidizing agents," Chem. Res. Toxicol. **10**, 386–392 (1997).
[58]M. P. Doyle and J. W. Hoekstra, "Oxidation of nitrogen oxides by bound dioxygen in hemoproteins," J. Inorg. Biochem. **14**, 351–358 (1981).
[59]J. S. Olson, "[38] stopped-flow, rapid mixing measurements of ligand binding to hemoglobin and red cells," Methods Enzymol. **76**, 631–651 (1981).
[60]S. Burney, J. L. Caulfield, J. C. Niles, J. S. Wishnok, and S. R. Tannenbaum, "The chemistry of DNA damage from nitric oxide and peroxynitrite," Mutat. Res., Fundam. Mol. Mech. Mutagen. **424**, 37–49 (1999).
[61]B. Roy, M. Lepoivre, Y. Henry, and M. Fontecave, "Inhibition of ribonucleotide reductase by nitric oxide derived from thionitrites: Reversible modifications of both subunits," Biochemistry **34**, 5411–5418 (1995).
[62]P. Howard-Flanders, "Effect of nitric oxide on the radiosensitivity of bacteria," Nature **180**, 1191–1192 (1957).
[63]L. H. Gray, F. O. Green, and C. A. Hawes, "Effect of nitric oxide on the radiosensitivity of tumour cells," Nature **182**, 952–953 (1958).
[64]D. L. Dewey, "Effect of oxygen and nitric oxide on the radiosensitivity of human cells in tissue culture," Nature **186**, 780–782 (1960).
[65]J. B. Mitchell, D. A. Wink, W. DeGraff, J. Gamson, L. K. Keefer, and M. C. Krishna, "Hypoxic mammalian cell radiosensitization by nitric oxide," Cancer Res. 53, 5845–5848 (1993).
[66]R. J. Griffin, C. M. Makepeace, W.-J. Hur, and C. W. Song, "Radiosensitization of hypoxic tumor cells *in vitro* by nitric oxide," Int. J. Radiat. Oncol., Biol., Phys. **36**, 377–383 (1996).
[67]B. F. Jordan, P. Sonveaux, O. Feron, V. Grégoire, N. Beghein, C. Dessy, and B. Gallez, "Nitric oxide as a radiosensitizer: Evidence for an intrinsic role in addition to its effect on oxygen delivery and consumption," Int. J. Cancer **109**, 768–773 (2004).
[68]P. Wardman, K. Rothkamm, L. K. Folkes, M. Woodcock, and P. J. Johnston, "Radiosensitization by nitric oxide at low radiation doses," Radiat. Res. **167**, 475–484 (2007).
[69]G. D. Stewart, J. Nanda, E. Katz, K. J. Bowman, J. G. Christie, D. G. Brown, D. B. McLaren, A. C. P. Riddick, J. A. Ross, G. D. D. Jones, and F. K. Habib, "DNA strand breaks and hypoxia response inhibition mediate the radiosensitisation effect of nitric oxide donors on prostate cancer under varying oxygen conditions," Biochem. Pharmacol. **81**, 203–210 (2011).
[70]S. Ning, M. Bednarski, B. Oronsky, J. Scicinski, G. Saul, and S. J. Knox, "Dinitroazetidines are a novel class of anticancer agents and hypoxia-activated radiation sensitizers developed from highly energetic materials," Cancer Res. **72**, 2600–2608 (2012).
[71]L. K. Folkes and P. O'Neill, "DNA damage induced by nitric oxide during ionizing radiation is enhanced at replication," Nitric Oxide **34**, 47–55 (2013).
[72]J. Tu, K. Tu, H. Xu, L. Wang, X. Yuan, X. Qin, L. Kong, Q. Chu, and Z. Zhang, "Improving tumor hypoxia and radiotherapy resistance via *in situ* nitric oxide release strategy," Eur. J. Pharm. Biopharm. **150**, 96–107 (2020).
[73]L. K. Keefer and D. A. Wink, in *Biological Reactive Intermediates V: Basic Mechanistic Research in Toxicology and Human Risk Assessment*, edited by R. Snyder *et al.* (Springer, Boston, MA, 1996), pp. 177–185.
[74]L. K. Folkes and P. O'Neill, "Modification of DNA damage mechanisms by nitric oxide during ionizing radiation," Free Radical Biol. Med. **58**, 14–25 (2013).
[75]Y. Sun, W. Zhou, M. M. Moe, and J. Liu, "Reactions of water with radical cations of guanine, 9-methylguanine, 2′-deoxyguanosine and guanosine: Keto-enol isomerization, C8-hydroxylation, and effects of N9-substitution," Phys. Chem. Chem. Phys. **20**, 27510–27522 (2018).
[76]Y. Fang and J. Liu, "Reaction of protonated tyrosine with electronically excited singlet molecular oxygen ($a^1\Delta_g$): An experimental and trajectory study," J. Phys. Chem. A **113**, 11250–11261 (2009).
[77]I. K. Chu, C. F. Rodriquez, T.-C. Lau, A. C. Hopkinson, and K. W. Michael Siu, "Molecular radical cations of oligopeptides," J. Phys. Chem. B **104**, 3393–3397 (2000).
[78]L. Feketeová, E. Yuriev, J. D. Orbell, G. N. Khairallah, and R. A. J. O'Hair, "Gas-phase formation and reactions of radical cations of guanosine, deoxyguanosine and their homodimers and heterodimers," Int. J. Mass Spectrom. **304**, 74–82 (2011).
[79]P. Cheng and D. K. Bohme, "Gas-phase formation of radical cations of monomers and dimers of guanosine by collision-induced dissociation of Cu(II)–guanosine complexes," J. Phys. Chem. B **111**, 11075–11082 (2007).
[80]A. Dang, Y. Liu, and F. Tureček, "UV–vis action spectroscopy of guanine, 9-methylguanine, and guanosine cation radicals in the gas phase," J. Phys. Chem. A **123**, 3272–3284 (2019).
[81]L. Feketeová, G. N. Khairallah, B. Chan, V. Steinmetz, P. Maître, L. Radom, and R. A. J. O'Hair, "Gas-phase infrared spectrum and acidity of the radical cation of 9-methylguanine," Chem. Commun. **49**, 7343–7345 (2013).
[82]F. Rogalewicz, Y. Hoppilliard, and G. Ohanessian, "Structures and fragmentations of zinc(II) complexes of amino acids in the gas phase. I. Electrosprayed ions which are structurally different from their liquid phase precursors," Int. J. Mass Spectrom. **201**, 307–320 (2000).
[83]F. Rogalewicz, G. Louazel, Y. Hoppilliard, and G. Ohanessian, "Structures and fragmentations of electrosprayed Zn(II) complexes of carboxylic acids in the gas phase: Isomerisation versus desolvation during the last desolvation step," Int. J. Mass Spectrom. **228**, 779–795 (2003).
[84]M. M. Moe, J. Benny, and J. Liu, "Collision-induced dissociation of homodimeric and heterodimeric radical cations of 9-methylguanine and 9-methyl-8-oxoguanine: Correlation between intra-base pair proton transfer originating from the N1–H at a Watson–Crick edge and non-statistical dissociation," Phys. Chem. Chem. Phys. **24**, 9263–9276 (2022).
[85]Y. Sun, M. M. Moe, and J. Liu, "Mass spectrometry and computational study of collision-induced dissociation of 9-methylguanine-1-methylcytosine base-pair radical cation: Intra-base-pair proton transfer and hydrogen transfer, non-statistical dissociation, and reaction with a water ligand," Phys. Chem. Chem. Phys. **22**, 14875–14888 (2020).
[86]K. M. Ervin and P. B. Armentrout, "Translational energy dependence of $Ar^+ + XY \rightarrow ArX^+ + Y$ (XY = $H_2$, $D_2$, HD) from thermal to 30 eV c.m.," J. Chem. Phys. **83**, 166–189 (1985).

04 September 2023 17:48:31


Published under an exclusive license by AIP Publishing

[87]P. B. Armentrout, "Mass spectrometry—Not just a structural tool: The use of guided ion beam tandem mass spectrometry to determine thermochemistry," J. Am. Soc. Mass Spectrom. **13**, 419–434 (2002).
[88]C. Rebick and R. D. Levine, "Collision induced dissociation: A statistical theory," J. Chem. Phys. **58**, 3942–3952 (1973).
[89]R. D. Levine and R. B. Bernstein, *Molecular Reaction Dynamics and Chemical Reactivity* (Oxford University Press, New York, 1987).
[90]P. B. Armentrout, "Kinetic energy dependence of ion–molecule reactions: Guided ion beams and threshold measurements," Int. J. Mass Spectrom. **200**, 219–241 (2000).
[91]J. Liu, B. van Devener, and S. L. Anderson, "Collision-induced dissociation of formaldehyde cations: The effects of vibrational mode, collision energy, and impact parameter," J. Chem. Phys. **116**, 5530–5543 (2002).
[92]P. J. Chantry, "Doppler broadening in beam experiments," J. Chem. Phys. **55**, 2746–2759 (1971).
[93]C. Lifshitz, R. L. C. Wu, T. O. Tiernan, and D. T. Terwilliger, "Negative ion–molecule reactions of ozone and their implications on the thermochemistry of $O_3^-$," J. Chem. Phys. **68**, 000247–260 (2008).
[94]M. B. Sowa-Resat, P. A. Hintz, and S. L. Anderson, "Dissociation energies for small carbon cluster ions ($C_{2-19}^+$) measured by collision-induced dissociation," J. Phys. Chem. **99**, 10736–10741 (1995).
[95]M. T. Rodgers, K. M. Ervin, and P. B. Armentrout, "Statistical modeling of collision-induced dissociation thresholds," J. Chem. Phys. **106**, 4499–4508 (1997).
[96]C. Lifshitz, "Kinetic shifts," Eur. J. Mass Spectrom. **8**, 85–98 (2002).
[97]R. A. Marcus, "Unimolecular dissociations and free radical recombination reactions," J. Chem. Phys. **20**, 359–364 (1952).
[98]A. Kumar and M. D. Sevilla, "Proton transfer induced SOMO-to-HOMO level switching in one-electron oxidized A-T and G-C base pairs: A density functional theory study," J. Phys. Chem. B **118**, 5453–5458 (2014).
[99]M. J. Frisch, G. W. Trucks, H. B. Schlegel, G. E. Scuseria, M. A. Robb, J. R. Cheeseman, G. Scalmani, V. Barone, G. A. Petersson, H. Nakatsuji, X. Li, M. Caricato, A. V. Marenich, J. Bloino, B. G. Janesko, R. Gomperts, B. Mennucci, H. P. Hratchian, J. V. Ortiz, A. F. Izmaylov, J. L. Sonnenberg, D. Williams-Young, F. Ding, F. Lipparini, F. Egidi, J. Goings, B. Peng, A. Petrone, T. Henderson, D. Ranasinghe, V. G. Zakrzewski, J. Gao, N. Rega, G. Zheng, W. Liang, M. Hada, M. Ehara, K. Toyota, R. Fukuda, J. Hasegawa, M. Ishida, T. Nakajima, Y. Honda, O. Kitao, H. Nakai, T. Vreven, K. Throssell, J. A. Montgomery, Jr., J. E. Peralta, F. Ogliaro, M. J. Bearpark, J. J. Heyd, E. N. Brothers, K. N. Kudin, V. N. Staroverov, T. A. Keith, R. Kobayashi, J. Normand, K. Raghavachari, A. P. Rendell, J. C. Burant, S. S. Iyengar, J. Tomasi, M. Cossi, J. M. Millam, M. Klene, C. Adamo, R. Cammi, J. W. Ochterski, R. L. Martin, K. Morokuma, O. Farkas, J. B. Foresman, and D. J. Fox, Gaussian 16, Revision B.01, Gaussian, Inc., 2016.
[100]M. Carla Aragoni, C. Caltagirone, V. Lippolis, E. Podda, A. M. Z. Slawin, J. Derek Woollins, A. Pintus, and M. Arca, "Diradical character of neutral heteroleptic bis(1,2-dithiolene) metal complexes: Case study of [Pd($Me_2$timdt)(mnt)] ($Me_2$timdt = 1,3-dimethyl-2,4,5-trithioxoimidazolidine; $mnt^{2-}$ = 1,2-dicyano-1,2-ethylenedithiolate)," Inorg. Chem. **59**, 17385–17401 (2020).
[101]I. M. Alecu, J. Zheng, Y. Zhao, and D. G. Truhlar, "Computational thermochemistry: Scale factor databases and scale factors for vibrational frequencies obtained from electronic model chemistries," J. Chem. Theory Comput. **6**, 2872–2887 (2010).
[102]E. D. Glendening, J. K. Badenhoop, A. E. Reed, J. E. Carpenter, J. A. Bohmann, C. M. Morales, C. R. Landis, and F. Weinhold, NBO 6.0, Theoretical Chemistry Institute, University of Wiscosin, 2013.
[103]T. J. Lee and P. R. Taylor, "A diagnostic for determining the quality of single-reference electron correlation methods," Int. J. Quantum Chem. **36**, 199–207 (1989).
[104]D. Jayatilaka and T. J. Lee, "Open-shell coupled-cluster theory," J. Chem. Phys. **98**, 9734–9747 (1993).
[105]D. G. Liakos, M. Sparta, M. K. Kesharwani, J. M. L. Martin, and F. Neese, "Exploring the accuracy limits of local pair natural orbital coupled-cluster theory," J. Chem. Theory Comput. **11**, 1525–1539 (2015).
[106]K. Raghavachari, G. W. Trucks, J. A. Pople, and M. Head-Gordon, "A fifth-order perturbation comparison of electron correlation theories," Chem. Phys. Lett. **157**, 479–483 (1989).
[107]F. Neese, "The ORCA program system," Wiley Interdiscip. Rev.: Comput. Mol. Sci. **2**, 73–78 (2012).
[108]F. Neese, "Software update: The ORCA program system, version 4.0," Wiley Interdiscip. Rev.: Comput. Mol. Sci. **8**, e1327 (2018).
[109]S. R. Huang and F. Tureček, "Cation radicals of hachimoji nucleobases P and Z: Generation in the gas phase and characterization by UV–vis photodissociation action spectroscopy and theory," J. Am. Soc. Mass Spectrom. **32**, 373–386 (2021).
[110]G. K. Jarvis, M. Evans, C. Y. Ng, and K. Mitsuke, "Rotational-resolved pulsed field ionization photoelectron study of $NO^+(X^1\Sigma^+, v^+ = 0–32)$ in the energy range of 9.24–16.80 eV," J. Chem. Phys. **111**, 3058–3069 (1999).
[111]C. Larriba and C. J. Hogan, Jr., "Free molecular collision cross section calculation methods for nanoparticles and complex ions with energy accommodation," J. Comput. Phys. **251**, 344–363 (2013).
[112]C. Larriba-Andaluz and C. J. Hogan, Jr., "Collision cross section calculations for polyatomic ions considering rotating diatomic/linear gas molecules," J. Chem. Phys. **141**, 194107 (2014).
[113]T. V. Ramakrishna Rao and R. Ramakrishna Reddy, "Potential energy curves and dissociation energy of the $NO^+$ molecule," Physica B+C **95**, 412–417 (1978).
[114]M. M. Moe, J. Benny, Y. Sun, and J. Liu, "Experimental and theoretical assessment of protonated Hoogsteen 9-methylguanine-1-methylcytosine base-pair dissociation: Kinetics within a statistical reaction framework," Phys. Chem. Chem. Phys. **23**, 9365–9380 (2021).
[115]J. Liu, B. W. Uselman, J. M. Boyle, and S. L. Anderson, "The effects of collision energy, vibrational mode and vibrational angular momentum on energy transfer and dissociation in $NO_2^+$-rare gas collisions: An experimental and trajectory study," J. Chem. Phys. **125**, 133115 (2006).
[116]R. M. Cox, K. Harouaka, M. Citir, and P. B. Armentrout, "Activation of $CO_2$ by actinide cations ($Th^+$, $U^+$, $Pu^+$, and $Am^+$) as studied by guided ion beam and triple quadrupole mass spectrometry," Inorg. Chem. **61**, 8168–8181 (2022).
[117]J. C. Rienstra-Kiracofe, W. D. Allen, and H. F. Schaefer III, "The $C_2H_5 + O_2$ reaction mechanism: High-level ab initio characterizations," J. Phys. Chem. A **104**, 9823–9840 (2000).
[118]T. J. Lee, "Comparison of the $T_1$ and $D_1$ diagnostics for electronic structure theory: A new definition for the open-shell $D_1$ diagnostic," Chem. Phys. Lett. **372**, 362–367 (2003).
[119]T. Saito, S. Nishihara, Y. Kataoka, Y. Nakanishi, T. Matsui, Y. Kitagawa, T. Kawakami, M. Okumura, and K. Yamaguchi, "Transition state optimization based on approximate spin-projection (AP) method," Chem. Phys. Lett. **483**, 168–171 (2009).
[120]T. Saito, S. Nishihara, Y. Kataoka, Y. Nakanishi, Y. Kitagawa, T. Kawakami, S. Yamanaka, M. Okumura, and K. Yamaguchi, "Reinvestigation of the reaction of ethylene and singlet oxygen by the approximate spin projection method. Comparison with multireference coupled-cluster calculations," J. Phys. Chem. A **114**, 7967–7974 (2010).
[121]H. Schwarz, "On the spin-forbiddeness of gas-phase ion–molecule reactions: A fruitful intersection of experimental and computational studies," Int. J. Mass Spectrom. **237**, 75–105 (2004).
[122]J. N. Harvey, "Understanding the kinetics of spin-forbidden chemical reactions," Phys. Chem. Chem. Phys. **9**, 331–343 (2007).
[123]Z. E. X. Dance, S. M. Mickley, T. M. Wilson, A. B. Ricks, A. M. Scott, M. A. Ratner, and M. R. Wasielewski, "Intersystem crossing mediated by photoinduced intramolecular charge transfer: Julolidine–anthracene molecules with perpendicular π systems," J. Phys. Chem. A **112**, 4194–4201 (2008).
[124]H. Cao, I. Kurganskii, J. Pang, R. Duan, J. Zhao, M. Fedin, M.-D. Li, and C. Li, "Charge transfer, intersystem crossing, and electron spin dynamics in a compact perylenemonoimide-phenoxazine electron donor–acceptor dyad," J. Phys. Chem. B **125**, 12859–12875 (2021).
[125]J. W. Verhoeven, "On the role of spin correlation in the formation, decay, and detection of long-lived, intramolecular charge-transfer states," J. Photochem. Photobiol., C **7**, 40–60 (2006).
[126]J. W. Verhoeven, H. J. van Ramesdonk, M. M. Groeneveld, A. C. Benniston, and A. Harriman, "Long-lived charge-transfer states in compact donor–acceptor dyads," ChemPhysChem **6**, 2251–2260 (2005).

04 September 2023 17:48:31


Published under an exclusive license by AIP Publishing

[127]Y. Zhao, R. Duan, J. Zhao, and C. Li, "Spin–orbit charge transfer intersystem crossing in perylenemonoimide–phenothiazine compact electron donor–acceptor dyads," Chem. Commun. **54**, 12329–12332 (2018).
[128]Y. Hou, I. Kurganskii, A. Elmali, H. Zhang, Y. Gao, L. Lv, J. Zhao, A. Karatay, L. Luo, and M. Fedin, "Electronic coupling and spin–orbit charge transfer intersystem crossing (SOCT-ISC) in compact BDP–carbazole dyads with different mutual orientations of the electron donor and acceptor," J. Chem. Phys. **152**, 114701 (2020).
[129]D. G. Torr and M. R. Torr, "Chemistry of the thermosphere and ionosphere," J. Atmos. Terr. Phys. **41**, 797–839 (1979).
[130]J. Kiviranta, K. Pérot, P. Eriksson, and D. Murtagh, "An empirical model of nitric oxide in the upper mesosphere and lower thermosphere based on 12 years of Odin SMR measurements," Atmos. Chem. Phys. **18**, 13393–13410 (2018).
[131]M. Ferus, F. Pietrucci, A. M. Saitta, A. Knížek, P. Kubelík, O. Ivanek, V. Shestivska, and S. Civiš, "Formation of nucleobases in a Miller–Urey reducing atmosphere," Proc. Natl. Acad. Sci. U. S. A. **114**, 4306–4311 (2017).
[132]Y. Oba, Y. Takano, Y. Furukawa, T. Koga, D. P. Glavin, J. P. Dworkin, and H. Naraoka, "Identifying the wide diversity of extraterrestrial purine and pyrimidine nucleobases in carbonaceous meteorites," Nat. Commun. **13**, 2008 (2022).

04 September 2023 17:48:31


Published under an exclusive license by AIP Publishing